PAPER • OPEN ACCESS

Effect of the isotope mass on pedestal structure, transport and stability in D, D/T and T plasmas at similar β_N and gas rate in JET-ILW type I ELMy H-modes

To cite this article: L. Frassinetti *et al* 2023 *Nucl. Fusion* **63** 112009

OPEN ACCESS
IOP Publishing | International Atomic Energy Agency
Nuclear Fusion
Nucl. Fusion **63** (2023) 112009 (30pp)
https://doi.org/10.1088/1741-4326/acf057

Effect of the isotope mass on pedestal structure, transport and stability in D, D/T and T plasmas at similar β_N and gas rate in JET-ILW type I ELMy H-modes

L. Frassinetti[1,*], C. Perez von Thun[2], B. Chapman-Oplopoiou[3], H. Nyström[1], M. Poradzinski[3], J.C. Hillesheim[3,a], L. Horvath[3], C.F. Maggi[3], S. Saarelma[3], A. Stagni[4,5], G. Szepesi[3], A. Bleasdale[3], A. Chomiczewska[2], R.B. Morales[3], M. Brix[3], P. Carvalho[3], D. Dunai[6], A.R. Field[3], J.M. Fontdecaba[7], H.J. Sun[3], D.B. King[3], D. Kos[3], E. Kowalska[2], B. Labit[8], M. Lennholm[3], S. Menmuir[3], E. Rachlew[1], D.I. Refy[6], P.A. Schneider[9], E.R. Solano[6], N. Vianello[4,10], M. Vécsei[6] and JET Contributors[11,b]

[1] Division of Fusion Plasma Physics, KTH Royal Institute of Technology, Stockholm, Sweden
[2] Institute of Plasma Physics and Laser Microfusion (IPPLM), Hery 23, 01-497 Warsaw, Poland
[3] CCFE, Culham Science Centre, Abingdon OX14 3DB, United Kingdom of Great Britain and Northern Ireland
[4] Consorzio RFX (CNR, ENEA, INFN, Università di Padova, Acciaierie Venete SpA), C.so Stati Uniti 4, 35127 Padova, Italy
[5] CRF-University of Padova, Italy
[6] Centre for Energy Research, Budapest, Hungary
[7] Laboratorio Nacional de Fusión, CIEMAT, Madrid, Spain
[8] École Polytechnique Fédérale de Lausanne (EPFL), Swiss Plasma Center (SPC), CH-1015 Lausanne, Switzerland
[9] Max-Planck-Institut für Plasmaphysik, Garching, Germany
[10] Istituto per la Scienza e la Tecnologia dei Plasmi, CNR, Padova, Italy
[11] EUROfusion Consortium, JET, Culham Science Centre, Abingdon OX14 3DB, United Kingdom of Great Britain and Northern Ireland

E-mail: lorenzof@kth.se

Received 3 March 2023, revised 21 July 2023
Accepted for publication 15 August 2023
Published 12 October 2023

Abstract

The work describes the pedestal structure, transport and stability in an effective mass (A_{eff}) scan from pure deuterium to pure tritium plasmas using a type I ELMy H-mode dataset in which key parameters that affect the pedestal behaviour (normalized pressure, ratio of the separatrix density to the pedestal density, pedestal ion Larmor radius, pedestal collisionality and rotation) are kept as constant as possible. Experimental results show a significant increase of the density at the pedestal top with increasing A_{eff}, a modest reduction in the temperature and an increase in the pressure. The variations in the pedestal heights are mainly due to a change in the pedestal gradients while only small differences are observed in the pedestal width. A clear increase in the pedestal density and pressure gradients are observed from deuterium to tritium. The

[a] Presently at Commonwealth Fusion Systems, 148 Sidney Street, Cambridge, MA 02139.
[b] See the author list of "Overview of T and D-T results in JET with ITER-like wall" by C.F. Maggi *et al* to be published in *Nuclear Fusion Special Issue: Overview and Summary Papers from the 29th Fusion Energy Conference (London, UK, 16–21 October 2023).*
[*] Author to whom any correspondence should be addressed.

experimental results suggest a reduction of the pedestal inter-edge localized mode (inter-ELM) transport from deuterium to tritium. The reduction is likely in the pedestal inter-ELM particle transport, as suggested by the clear increase of the pedestal density gradients. The experimental results suggest also a possible reduction of the pedestal inter-ELM heat transport, however, the large experimental uncertainties do not allow conclusive claims on the heat diffusivity. The clear experimental reduction of η_e (the ratio between density and temperature gradient lengths) in the middle/top of the pedestal with increasing A_{eff} suggests that there may be a link between increasing A_{eff} and the reduction of electron scale turbulent transport. From the modelling point of view, an initial characterization of the behaviour of pedestal microinstabilities shows that the tritium plasma is characterized by growth rates lower than the deuterium plasmas. The pedestal stability of peeling-ballooning modes is assessed with both ideal and resistive magnetohydrodynamics (MHD). No significant effect of the isotope mass on the pedestal stability is observed using ideal MHD. Instead, resistive MHD shows a clear increase of the stability with increasing isotope mass. The resistive MHD results are in reasonable agreement with the experimental results of the normalized pedestal pressure gradient. The experimental and modelling results suggest that the main candidates to explain the change in the pedestal are a reduction in the inter-ELM transport and an improvement of the pedestal stability from deuterium to tritium.

Keywords: pedestal, stability, tritium, deuterium/tritium, JET-ILW, isotope effect

(Some figures may appear in colour only in the online journal)

1. Introduction

ITER and future fusion reactors will operate with mixed deuterium/tritium plasmas. It is therefore essential to understand the dependence of the confinement on the isotope mass as this will improve our predictive capabilities and will lead us to more reliable and robust predictions of future burning plasmas.

The only experiments with pure tritium (T) and mixed deuterium/tritium (D/T) plasmas have been performed in the 1990s in TFTR and in JET with a carbon wall (hereafter JET-C) [1, 2]. While the underlying physics that describes the effect of the isotope mass on the confinement is not fully understood, the major advances made both in theory and in experimental diagnostics in the past 25 years have the potential to identify the key physics mechanisms related to the effect of the isotope mass. Moreover, while earlier experimental results with D/T and T plasmas are from carbon wall machines, ITER will operate with a metal wall composed of beryllium in the main chamber and tungsten in the divertor. To assess the possible effect of the wall materials, in 2011 JET has changed its wall from carbon to beryllium and tungsten, to mimic a ITER-like wall (here after JET-ILW) [3]. The initial JET-ILW results have shown a lower pedestal temperature in baseline plasmas, likely produced by operation with higher gas rate [4–6] and different intrinsic impurities [7–10]. Therefore, it was not obvious how a D/T and a T plasma would have behaved in a metal wall machine. For these reasons, the time was ripe for a new experimental campaign with D/T and T plasmas. The campaign was performed in 2021 and 2022 with, among the key objectives, the goal of exploiting the new JET diagnostics and the most recent theoretical developments to identify the physics mechanisms that can explain the effect of the isotope mass on the plasma confinement.

In literature, regression analysis between the energy confinement time τ_E and the isotope mass A have been performed including both hydrogen (H) plasmas, D, D/T and T plasmas. In general, a favourable dependence of τ_E with A has been experimentally observed, both in L-mode plasmas and in H-mode plasmas and both in tokamaks and stellarators [11–20]. In H-mode, the most well-known result is the IPB98(y,2) scaling which is a multi-machine regression analysis described in the ITER physics basis [21] and obtained with a multi-variable power law fit. In the IPB98(y,2) scaling, τ_E increases with the isotope mass as $\tau_E \propto A^{0.19}$. The correlation was much weaker when considering only a subset of type I ELMy H-mode JET-C plasmas at similar density, with $\tau_E \propto A^{0.03}$ [22]. This was due to the compensation of a strong positive correlation for the pedestal stored energy W_{ped} ($W_{ped} \propto A^{0.96}$) by a negative correlation with isotope mass for the core energy confinement ($\tau_{core} \propto A^{-0.16}$). A recent work, that included the 1997 plasmas with T and D/T, has ascribed the weak exponent of the JET-C dataset to a correlation between density and isotope mass [23]. A recent revision of the ITPA confinement database, which included new hydrogen data from JET-ILW and ASDEX-Upgrade (AUG), has also led to a positive correlation between energy confinement and isotope mass, with $\tau_E \propto A^{\alpha_A}$ and α_A in the range $0.09 - 0.47$ (depending on the dataset and the regression technique) [24].

Due to lack of pedestal diagnostics in the JET 1997 D/T experimental campaign, the majority of the pedestal results related to the effect of the isotope mass are from H and D plasmas. In JET-ILW H and D plasmas, a dependence of τ_E versus A stronger than the IPB98(y,2) scaling has been observed in type I ELMy H-mode, with $\tau_E \propto A^{0.4}$ [11, 25]. This was ascribed to a pedestal effect. While the electron temperature (T_e) gradient length ($L_{T_e} = T_e/\nabla T_e$) in the core was similar between H and D plasmas with same engineering parameters, the electron pedestal pressure (p_e^{ped}) was higher in D than in H due to a higher electron pedestal density (n_e^{ped}) [11, 26, 27]. This is consistent with AUG results, where an increased

pedestal confinement from H to D has been ascribed as well to the n_e^{ped} increase [18, 27, 28]. Interestingly, in JT-60U the positive correlation between energy confinement and isotope mass was observed only in the core, with no clear effect of the isotope mass on the pedestal [12–14]. In particular, a hydrogen plasma and a deuterium plasma with same current, toroidal field, shape and thermal stored energy were showing a very similar pedestal [14]. Minor differences in the pedestal structure between hydrogen and deuterium plasmas have been reported also for DIII-D when performing a comparison between discharges with same current, field, shape and β_N [29].

At present, no complete explanation for the effect of the isotope mass on the pedestal is available. In particular, ideal magnetohydrodynamics (MHD) predicts only a negligible effect of the isotope mass on the pedestal stability of the peeling-ballooning (PB) modes, as shown in JET-ILW by studying H and D in type I ELMy H-mode plasmas [26, 27]. However, the field is progressing fast. From an experimental point of view, results in AUG from density fluctuations obtained via Doppler reflectometry might suggest an enhanced inter-edge localized mode (inter-ELM) transport in H plasmas [28]. These might be consistent with recent turbulent transport modelling performed with GENE in H and D JET-ILW type I ELMy H-modes [30], where lower inter-ELM turbulent particle transport is found in deuterium than in hydrogen. A reduction of the particle transport with increasing isotope mass would be qualitatively consistent with the experimentally observed higher n_e^{ped} in deuterium than in hydrogen selected pedestals [11, 26–28].

The recent experimental results in H and D described above show that the pedestal plays a key role in understanding the effect of the isotope mass on confinement. The present work is based on the recent JET-ILW D/T and T experimental campaign and describes the effect of the isotope mass on the pedestal in D, D/T, and T in type I ELMy H-mode plasmas. The work exploits state of the art pedestal diagnostics to describe the pedestal structure in D, D/T and T and the most recent theoretical models to identify the possible physics mechanisms behind the effect of the isotope mass in the JET-ILW pedestal. Particular emphasis is given to the pedestal stability, a key ingredient for the pedestal predictions. However, disentangling the effect of the isotope mass from that of other physics parameters is challenging. In type I ELMy H-modes, inter-ELM pedestal transport (that is considered a soft limit for the gradients) and pedestal stability of PB MHD modes (that determines the ELM triggering mechanism) are affected by multiple parameters. Special care has been taken to obtain a dataset that allows the assessment of the direct effect of the isotope mass on the pedestal.

The paper is organized as follows. Section 2 describes the dataset and the motivation behind its choice. Section 3 presents the key diagnostics and the experimental data analysis technique. Section 4 presents an overview of the global properties of the dataset, such as stored energy, energy confinement, absorbed power and ELM type. Then, the work investigates in detail the pedestal behaviour, first from the experimental point of view, then from a theoretical point of view. Given that the present predictive models for type I ELMs rely on the physics of pedestal transport and pedestal stability, the work will to try to assess both. Section 5 describes the pedestal structure of electron density n_e, temperature T_e and pressure p_e. Section 6 discusses the ELM energy losses. Section 7 describes experimental results related to the transport. Section 8 applies a recent predictive model for the pedestal density to the present dataset. The section tests if, and under which assumptions, the model can predict the n_e^{ped} variation between D, D/T and T plasmas. Section 9 characterizes the type of micro-instabilities in the pedestal of the D and T pulses via gyrokinetic modelling performed with the GENE code. Section 10 describes the PB stability of the D, D/T and T dataset, with particular emphasis on the differences between ideal and resistive MHD. Finally, section 11 presents discussion and conclusions.

2. The experimental dataset

2.1. Motivation for the choice of the dataset

The ultimate goal of this work is to shed light on the physics mechanisms that can explain the effect of the isotope mass on the pedestal. The pedestal properties are determined by two key mechanisms. One is the transport of energy and particles, which sets the pedestal gradients and affects the inter-ELM time evolution. The other is the pedestal stability, which determines the ELM triggering mechanism. Both transport and stability are affected by a large number of parameters. In type I ELMy H-modes, two key plasma parameters that affect pedestal transport and stability are the normalized pressure β_N [31] and the ratio between the separatrix density and the pedestal density (n_e^{sep}/n_e^{ped}) [32–36]. Other parameters such as the normalized ion Larmor radius ρ^* and the normalized collisionality ν^* can also affect the pedestal transport and/or the pedestal stability [31], however only large variations of ρ^* and ν^* can have a significant effect on the pedestal (see, for example, the JET-ILW results on dimensionless scans in ρ^* and ν^* discussed in [37, 38]). From an engineering point of view, the parameters I_p, B_t, gas rate, power, plasma shape, strike point position and divertor configuration can also affect the pedestal. In large part, the engineering parameters affect the pedestal in an indirect way, for example via their effect on β_N, n_e^{sep}/n_e^{ped}, ρ^* and ν^*. As an example, the input power can act on the pedestal via its effect on β_N [31].

Therefore, identifying the direct effect of the isotope mass on the pedestal is not trivial. Comparing D and T plasmas with identical engineering parameters would lead to plasmas with different β_N, n_e^{sep}/n_e^{ped}, ρ^* and ν^*. It would not be obvious how to disentangle the effect of the isotope mass on the pedestal from that of β_N, n_e^{sep}/n_e^{ped}, ρ^* and ν^*. For this reason, this work is based on specific discharges which have been performed to obtain an isotope mass scan characterized by β_N, n_e^{sep}/n_e^{ped}, ρ^*, ν^* as similar as possible. Given that ρ^* and ν^* affect the pedestal only if their variation is very large, the pulses used in this work have been performed at similar β_N (by operating the NBI in feedback) and at constant n_e^{sep}/n_e^{ped} (by keeping the gas rate constant) but by changing the isotope mass. As described

in section 2.2, this has indirectly led also to a constant pedestal ρ^* and to only a small variation in the pedestal ν^*. The dataset is therefore optimal to assess the direct effect of the isotope mass on the pedestal structure, transport and stability.

2.2. The experimental dataset

2.2.1. The A_{eff} scan dataset. The key dataset used in this work is an isotope mass scan at similar β_N and constant gas rate in type I ELMy H-modes (the ELM type will be discussed in section 4). Hereafter, the dataset is called 'A_{eff} scan dataset' (see expression (1) for the A_{eff} definition). The A_{eff} scan dataset is composed of six pulses in which the plasma isotopic composition has been changed from shot to shot from D to T and in which the NBI has been operated in feedback to keep β_N as constant as possible ($\beta_N \approx 1.5$). Apart from the NBI power and the isotopic composition, the other engineering parameters have been kept as constant as possible. The engineering parameters are shown in table 1. All pulses have $I_p/B_t = 2\text{MA}/2.25\text{T}$, gas rate $\Gamma \approx 1.7 \times 10^{22}$ (e s^{-1}) injected from the divertor, low triangularity, inner strike point on the vertical target and outer strike point on the horizontal target. The line averaged density measured from a line of sight that intersects the core is also shown in table 1.

The requested ICRH power (used to avoid impurity accumulation in the core) is 2 MW. The RF antenna could not always deliver a constant power on a shot to shot basis, but this was compensated by the NBI that was operating in feedback to keep $\beta_N \approx 1.5$. The plasma isotopic composition has been varied from pure D to pure T. The plasma isotopic composition has been quantified via the effective mass A_{eff}:

$$A_{eff} = \frac{c_H A_H + c_D A_D + c_T A_T}{c_H + c_D + c_T} \quad (1)$$

where A_H, A_D, A_T are the relative atomic masses $A_i = m_i/m_p$ of hydrogen, deuterium and tritium respectively and c_H, c_D, c_T are the concentrations of H, D, T. In the dataset, the hydrogen concentration is very small, around 1%–2%, and it is used for the ICRH heating.

To ensure the robustness of the results, two D pulses have been used. The first D pulse (#96208) was taken before the D/T campaign while the second D pulse (#100808) was taken after. The two deuterium pulses have identical engineering parameters apart from a 4.5 cm difference in the outer strike position (however, still located on the horizontal target in both cases). As later discussed in sections 4 and 5, this difference leads to a negligible variation in the pedestal structure (variation that is, in any case, much smaller than the difference between D and T plasmas).

The A_{eff} scan dataset is composed also of one pure T plasma and three D/T plasmas. Due to the strict limits in the T gas consumption and in the neutron budget, it was not possible to perform further pulses.

The A_{eff} scan dataset is highlighted throughout this work using full symbols with a black outline. In detail, the T pulse is represented with a magenta star, the D/T pulses with gold circles and the D pulses with blue squares (#96208 filled with a small white square). Figure 1 shows an overview of the A_{eff} scan dataset. Figure 1(*a*) shows the effective mass which varies between 2 and 3, and the gas rate, which is constant at $\Gamma \approx 1.7 \times 10^{22}$ (e s^{-1}). Figure 1(*b*) shows β_N versus the absorbed power P_{abs}. The absorbed power has been defined as the total input power including ohmic power, ICRH power and NBI power (with the shine through excluded). A higher P_{abs} is necessary in D plasmas than in T plasmas in order to keep β_N constant. As discussed in section 4, this is due to an increase in the energy confinement from D to T.

To obtain plasmas with similar β_N, the NBI was operated in feedback. Only discrete P_{NBI} steps are possible, each step size being ≈10% the total applied NBI power, so roughly a ±5% variation in β_N can be expected. Indeed, the resulting β_N is in the range 1.44–1.58. This variation is small enough not to affect significantly the pedestal and the conclusion of the work.

The NBI system in JET is composed of two injectors, each one consisting of eight ion sources (PINIs). Each injector has four PINIs oriented in a normal beam bank (tangential radii 1.31 m) and four PINIs oriented in a tangential beam bank (tangential radii 1.85 m). All the mixed D/T plasmas in the A_{eff} scan dataset are equally heated by the normal PINIs and by the tangential PINIs. The pure T pulse #100247 is heated 80% by the normal PINIs and 20% by the tangential PINIs. The deuterium pulse #96208 has a heating mix similar to the T pulse. The deuterium pulse #100808 has a heating mix similar to the D/T pulses. As later described, the two D pulses do not show any significant difference in the confinement and in the pedestal between themselves while they show the same difference with respect to the T pulse. So, the variation in the mix of beams cannot affect our conclusions. As a final remark on the heating scheme, the ratio P_{ICRH}/P_{NBI} varies from 0.17 in the D pulses to 0.11 in the T pulse. This variation cannot significantly influence our conclusions since, in JET, the ratio P_{ICRH}/P_{NBI} does not have any major effect on the energy confinement and on the pedestal behaviour, as shown in [39].

The main plasma parameters that can affect pedestal transport and pedestal stability are shown in table 2. As already mentioned, the plasmas have similar β_N. Moreover, the gas rate (including the fuelling location) and strike positions have also been kept constant to minimize the variation of n_e^{sep}/n_e^{ped}. Indeed, n_e^{sep}/n_e^{ped} is relatively constant at ≈0.5 (see also section 5). The exception is the D pulse #96208 which is characterized by $n_e^{sep}/n_e^{ped} \approx 0.65$. The higher n_e^{sep}/n_e^{ped} in #96208 might be related to either the slightly different strike point position or to a different wall condition. As discussed in this work and in earlier works [36], this difference in n_e^{sep}/n_e^{ped} is so small that leads only to minimal effects on the pedestal transport and stability (showing that slightly different strike point positions and wall recycling cannot affect significantly our conclusions). Table 2 reports also the normalized ion Larmor radius at the pedestal top. Due to the presence of mixed D/T plasmas, an effective ion Larmor radius has been used, defined as $\rho_i^{*ped} = \sqrt{A_{eff} T_i^{ped}}/(eBa)$. ρ_i^{*ped} is rather constant with a variation in the range $2.1 - 2.3 \times 10^{-3}$. As described in section 5, T_i^{ped} tends to weakly decrease from D to

Table 1. Main engineering parameters for the main dataset, showing effective mass, I_p, B_T, NBI power, ICRH power, average triangularity, inner/outer strike point position (where V stands for vertical target and H for horizontal target) and line averaged density.

Pulse	$A_{\rm eff}$	I_p/B_T (MA/T)	Γ (e/s)	$P_{\rm NBI}$ (MW)	$P_{\rm ICRH}$ (MW)	δ	Strike points	$\bar{n}_{\rm e}$ $\left(\rm m^{-3}\right)$
#96208	2.0	2/2.25	1.7×10^{22}	15	2.5	0.24	V/H	4.3×10^{19}
#100808	2.0	2/2.25	1.8×10^{22}	15	2.2	0.24	V/H	4.6×10^{19}
#99480	2.2	2/2.25	1.7×10^{22}	15	0	0.24	V/H	5.2×10^{19}
#99491	2.4	2/2.25	1.6×10^{22}	14	2.3	0.24	V/H	5.7×10^{19}
#99490	2.7	2/2.25	1.7×10^{22}	13	1.9	0.24	V/H	6.0×10^{19}
#100247	3.0	2/2.25	1.7×10^{22}	11	1.2	0.24	V/H	6.3×10^{19}

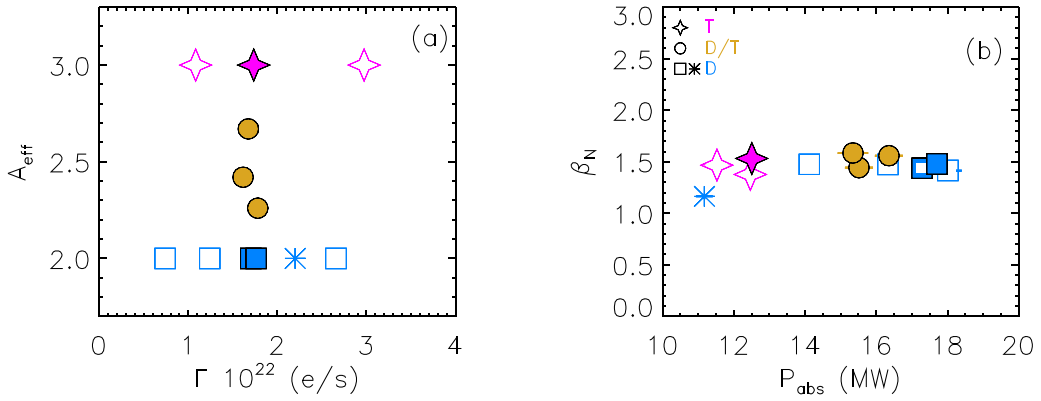

Figure 1. Characterization of the datasets in terms of effective mass and gas rate (*a*), and $\beta_{\rm N}$ and absorbed power (*b*). The $A_{\rm eff}$ scan dataset is highlighted by full symbols with a black outline, the extended dataset by empty symbols. The blue asterisk highlights pulse #96418 with engineering parameters and $P_{\rm sep}$ similar to the T pulse #100247. Throughout the work, T pulses are highlighted with magenta stars, D/T pulses with gold circles and D pulses with blue squares.

T (see section 3.1 for the details on $T_{\rm i}^{\rm ped}$ measurements). This decrease is compensated by the increase of $A_{\rm eff}$, leading to the relatively constant $\rho_{\rm i}^{*\rm ped}$. Instead, it was not possible to keep constant the pedestal ion-electron normalized collisionality $\nu_{\rm e}^{*\rm ped} = 6.921 \cdot 10^{-18} \ln\Lambda (R q_{95} n_{\rm e}^{\rm ped})/(\varepsilon^{3/2} \left(T_{\rm e}^{\rm ped}\right)^2)$, where $\ln\Lambda$ is the Coulomb logarithm and ε the inverse aspect ratio. The collisionality increases by a factor two from $\nu_{\rm e}^{*\rm ped} \approx 0.8$ in D to $\nu_{\rm e}^{*\rm ped} \approx 1.8$ in T (this is due to an increase in the pedestal density and a decrease in the pedestal temperature, as discussed in section 5). In principle, this variation could affect the pedestal transport and the pedestal bootstrap current, therefore harming the goal of the work to assess the direct effect of the isotope mass on the pedestal. However, earlier experimental results show that only large variations in $\nu_{\rm e}^{*\rm ped}$ can have a major effect on the pedestal. For example, from a dimensionless collisionality scan performed in JET-ILW, the electron pressure pedestal width $w_{\rm pe}$ scales approximately as $w_{\rm pe} \propto (\nu_{\rm e}^{*\rm ped})^{0.25}$ [37]. A factor of two variation in the collisionality leads only to a 18% variation in the width (which is only marginally higher than the experimental uncertainty). Also in terms of pedestal stability a significant effect can occur only with large variation of pedestal collisionality. From a set of dimensionless scans in JET-ILW [38], the critical pedestal pressure gradient ($\alpha_{\rm crit}$) scales with collisionality approximately as $\alpha_{\rm crit} \propto (\nu_{\rm e}^{*\rm ped})^{-0.14}$. So, a factor of two variation in collisionality can be expected to affect $\alpha_{\rm crit}$ in JET-ILW by only 10% (smaller than the experimental uncertainties in the normalized pressure gradient). It is worth anticipating that the present work will show that the increasing $A_{\rm eff}$ leads to a higher pedestal pressure and improves the pedestal stability. Therefore, keeping $\nu_{\rm e}^{*\rm ped}$ constant would have led only to an amplification of these effects and would not have changed the qualitative conclusions of the work. For these reasons, it is judged that such a variation in $\nu_{\rm e}^{*\rm ped}$ might have only a minor quantitative effect on our conclusions.

2.2.2. The extended dataset. To clarify some aspects of the results achieved with the $A_{\rm eff}$ scan dataset, some parts of the work have been complemented with an extended dataset.

One pulse of the extended dataset (#96418) is in deuterium. It has been selected to have the power through the separatrix ($P_{\rm sep}$, see section 4 and figure 4) and the other engineering parameters as similar as possible to the tritium pulse #100247 from the $A_{\rm eff}$ scan. Its engineering and plasma parameters are reported at the top of tables 3 and 4. This pulse is used in all the figures of the paper along with the $A_{\rm eff}$ scan dataset and it is highlighted using a blue asterisk. The gas rate of #96418 is slightly higher than in #100247 as can be seen in figure 1(*a*), but this small difference should not affect significantly our conclusions. Note that, since the D pulse #96418 has $P_{\rm sep}$ similar to the T pulse #100247, the values of $\beta_{\rm N}$ are different (figure 1(*b*)) due to the improved energy confinement with increasing $A_{\rm eff}$.

Then, further five pulses have been considered when discussing the ELM type (figure 5) and the possible role

Table 2. Key plasma parameters for the main dataset.

Pulse	*Isotope*	$A_{\rm eff}$	$\beta_{\rm N}$	$n_{\rm e}^{\rm sep}/n_{\rm e}^{\rm ped}$	$\nu_{\rm e}^{*\rm ped}$	$\rho_{\rm i}^{*\rm ped}\left(10^{-3}\right)$
#96208	D	2.0	1.44	0.65	0.7	2.2
#100808	D	2.0	1.47	0.52	0.9	2.1
#99480	D/T	2.2	1.45	0.52	1.0	2.2
#99491	D/T	2.4	1.55	0.46	1.1	2.2
#99490	D/T	2.7	1.58	0.48	1.5	2.2
#100247	T	3.0	1.53	0.52	1.8	2.3

Table 3. Main engineering parameters for the extended dataset, showing effective mass, I_p, B_T, NBI power, ICRH power, average triangularity, inner/outer strike point position (where V stands for vertical target and H for horizontal target) and line averaged density.

Pulse	$A_{\rm eff}$	I_p/B_T (MA/T)	Γ (e/s)	$P_{\rm NBI}$ (MW)	$P_{\rm ICRH}$ (MW)	δ	Strike points	$\bar{n}_{\rm e}\left({\rm m}^{-3}\right)$
#96418	2.0	2/2.25	2.2×10^{22}	8	2.3	0.24	V/H	5.0×10^{19}
#100183	3.0	2/2.25	2.9×10^{22}	9	2.2	0.24	V/H	8.2×10^{19}
#100185	3.0	2/2.25	1.1×10^{22}	9	1.4	0.24	V/H	5.6×10^{19}
#96201	2.0	2/2.25	2.6×10^{22}	16	2.4	0.24	V/H	4.7×10^{19}
#96202	2.0	2/2.25	0.7×10^{22}	12	2.2	0.24	V/H	4.2×10^{19}
#96197	2.0	2/2.25	0.7×10^{22}	15	1.1	0.24	V/H	4.4×10^{19}

Table 4. Key plasma parameters for the extended dataset.

Pulse	Isotope	$A_{\rm eff}$	$\beta_{\rm N}$	$n_{\rm e}^{\rm sep}/n_{\rm e}^{\rm ped}$	$\nu_{\rm e}^{*\rm ped}$	$\rho_{\rm i}^{*\rm ped}\left(10^{-3}\right)$
#96418	D	2.0	1.16	0.57	1.4	2.4
#100183	T	3.0	1.38	0.70	7.3	2.2
#100185	T	3.0	1.47	0.42	1.2	3.2
#96201	D	2.0	1.42	0.70	0.8	2.7
#96202	D	2.0	1.47	0.42	0.4	3.1
#96197	D	2.0	1.47	0.53	0.6	2.9

of the ELM frequency in determining the pedestal density (figure 20). The engineering and plasma parameters of these pulses are reported in tables 3 and 4. Three pulses are in deuterium and two in tritium. They have the same I_p, B_t, plasma shape, strike point position, $\beta_{\rm N}$ and gas fuelling location as the $A_{\rm eff}$ scan dataset. These five pulses are shown only in figures 1, 5 and 20. They are highlighted using open symbols.

3. Diagnostics and experimental data analysis technique

3.1. Diagnostics

The pedestal structure has been studied using the main diagnostics available. The key diagnostic used is the high resolution Thomson scattering (HRTS) which measures simultaneously electron temperate $T_{\rm e}$ and density $n_{\rm e}$ [40] at 20 Hz. Due to its high spatial resolution, the HRTS is very valuable to determine the pre-ELM pedestal structure. For the electron density pre-ELM profiles, the HRTS information have been complemented with the Lithium beam [41] which provides high quality profiles in the scrape off layer (SOL) at 100 Hz. However, the Lithium beam does not reach the pedestal top in these pulses (for details, see [41]). For the electron temperature pre-ELM profiles, the HRTS values at the pedestal top have been cross checked with the ECE. A good agreement has been found. Unfortunately, the ECE can reach only the middle/top of the pedestal and no information on the gradient can be obtained due to the insufficient spatial resolution. So, in terms of pre-ELM profiles the ECE was used only to cross-check the HRTS data. The pre-ELM ion temperature profiles, $T_{\rm i}$, have been measured with the core and edge charge exchange spectroscopy (CXRS). CXRS provides ion temperature and toroidal rotation of the main impurity which, in these plasmas, is neon (trace neon puffs have been used). The core and edge CXRS provide data with a 33 Hz and 20 Hz time resolution respectively. An example of $T_{\rm e}$ and $T_{\rm i}$ comparison is shown in figure 2 (which will be discussed later in this section).

The effective mass has been measured from the sub-divertor neutral gas pressure via spectral analysis of D_α and T_α emission from a penning gauge. This type of measurement agrees very well with that from spectroscopy obtained by comparing the relative amplitude of the Balmer D_α and T_α spectral lines from the plasma edge. These edge estimates are also consistent with the core effective mass estimated by modelling the isotope ratio with TRANSP (both in mixed H/D plasmas [42] and in mixed D/T plasmas [43]). As shown in [42], the three estimates of $A_{\rm eff}$ agree within 5%. Moreover, tritium plasmas with high purity have been obtained during the pure T campaign thanks to the low fuel retention of the JET-ILW metallic walls [44] and thanks to a two-step isotope-changeover (first from deuterium to hydrogen and then from hydrogen to tritium) [45].

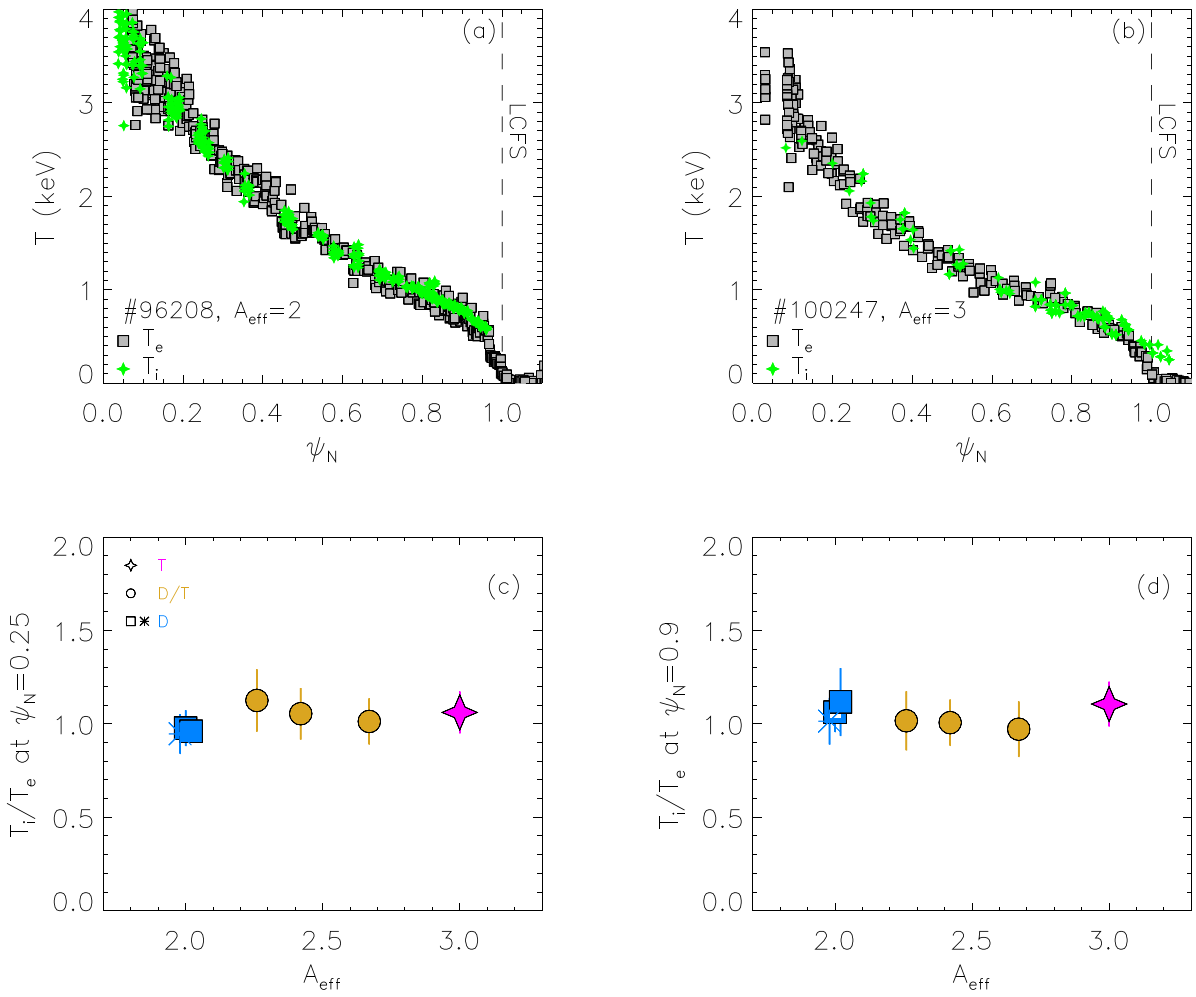

Figure 2. Pre-ELM electron temperature (grey squares) and ion temperature (green stars) for the D pulse #96208 (*a*) and the T pulse #100247 (*b*). Frames (*c*) and (*d*) show the ratio of T_i/T_e determined respectively in the core, at $\psi_N = 0.25$, and near the pedestal top, at $\psi_N = 0.9$.

3.2. Experimental data analysis technique

The pre-ELM profiles of n_e and T_e have been determined with the approach described in detail in [46] , where all the pre-ELM profiles in a steady time interval have been considered (at least 0.5 s long, i.e. at least two energy confinement times long). The pre-ELM profiles have been defined as those located in the 70%–99% of the ELM cycle. The composite HRTS profile for the D pulse #96208 and the T pulse #100247 are shown in figure 2 with grey squares. The same approach has been used for the Li-beam data and the CX data. An example of the pre-ELM T_i data can be found in figure 2 as green stars. From the core to the pedestal top, $T_i = T_e$ both in the D pulse and in the T pulse. This has been quantified in figure 2(*c*), where T_i/T_e in the core is shown for the A_{eff} scan dataset, and in figure 2(*d*), where T_i/T_e near the pedestal top is shown. Within the error bars, $T_i = T_e$ for the entire dataset from the core to the pedestal top. As well known, at the separatrix we can expect $T_i > T_e$. Unfortunately, T_i measurements at the separatrix are not available for the entire dataset. However, when available it was confirmed by the edge CX that $T_i > T_e$, as shown for example for the T pulse in figure 2(*b*). Due to the uncertainty in the exact separatrix position, firm conclusions on the value of T_i^{sep} are not possible. However, based on the experimental measurement for the T and the D/T pulses we can set $T_i^{sep} = 400\,eV$ as an upper bound. In the modelling results of the following sections (TRANSP, GENE and pedestal stability) sensitivity tests have been performed assuming as the two extreme values $T_i^{sep} = T_e^{sep}$ and $T_i^{sep} = 400\,eV$.

The information on the pedestal structure has been determined by fitting the composite pre-ELM profile of T_e and p_e with a modified hyperbolic tangent (*mtanh*) [47]. This approach works very well with T_e and p_e since in the SOL the experimental data are very close to zero. However, the density is non-negligible in the SOL so a slightly more sophisticated approach has been used. The HRTS data have been complemented with the Li-beam data which provides good quality SOL density. The pre-ELM Li-beam data have been manually aligned to have the pedestal gradient in the same position as the HRTS. However, the radial shift was relatively small, less 0.5 cm (likely due to small uncertainties in the equilibrium reconstruction). Then, the composite density profile is fitted with a modified hyperbolic tangent that contains a slope also in the SOL [37]. Note that the definition of the width used

in this work corresponds to the pedestal width of the whole density profile, not only the region inside the separatrix. An example of the pedestal profiles and the fits can be found in section 5. The reflectometry data were not included in this process because the absolute position of each single reflectometry profile is rather uncertain and their inclusion would not have improved the accuracy of the analysis.

The effective charge $Z_{\rm eff}$ is a line averaged value and is measured by visible Bremsstrahlung. The D pulse #96208 has $Z_{\rm eff} \approx 1.7$. Unfortunately, the uncertainty in $Z_{\rm eff}$ is rather large for the D/T and T plasmas. Therefore, both in the TRANSP modelling and in the pedestal stability analysis, a wide sensitivity test in $Z_{\rm eff}$ has been done (in the range of $Z_{\rm eff} = 1.2 - 2.0$), showing that the qualitative conclusions of the work are not affected.

The diagnostics have been mapped on the normalized poloidal flux ($\psi_{\rm N}$) using the best available equilibrium from EFIT++ determined with the full set of available magnetic measurements (which has been shown to improve the computed LCFS location [48]). To remove possible uncertainties in the pedestal position of the experimental data, in JET-ILW the pre-ELM profiles are typically shifted to have 100 eV at the separatrix. Due to the improved equilibrium used in this work, the shift is very small. However, in this work we have used an approach as realistic as possible, by determining $T_{\rm e}^{\rm sep}$ on a shot to shot basis using the two point model [49] combined with λ_q estimation from the Eich scaling [50]. Using this approach, $T_{\rm e}^{\rm sep}$ is relatively constant and varies in the range $T_{\rm e}^{\rm sep} \approx 120\,$eV for the D pulse #96208 to $T_{\rm e}^{\rm sep} \approx 110\,$eV for the T pulse #100247. In this work (excluding only section 9, see later for details), the pre-ELM profiles have been radially shifted to have the two point model $T_{\rm e}^{\rm sep}$. It has been shown in several previous works that such a variation in $T_{\rm e}^{\rm sep}$ does not lead to any significant difference from the usual JET assumption $T_{\rm e}^{\rm sep} = 100\,$eV [35, 36, 51]. Nonetheless, careful sensitivity tests have been done, in particular for the section related to the pedestal stability analysis where it is confirmed that a $T_{\rm e}^{\rm sep}$ variation in the range 100 eV–120 eV cannot affect the conclusion of the work.

4. Overview of energy confinement, power through the separatrix and ELM type

4.1. Thermal stored energy and energy confinement

The thermal energy confinement $\tau_{\rm E}^{\rm th}$ has been determined as the ratio between the thermal stored energy $W_{\rm th}$ and the loss power $P_{\rm loss}$.

The thermal stored energy $W_{\rm th}$ has been calculated by volume integrating the kinetic profiles using $T_{\rm i} = T_{\rm e}$ (assumption verified in figure 2) and calculating the ion density as $n_{\rm i} = n_{\rm e}\left(Z_{\rm main} + 1 - Z_{\rm eff}\right)/Z_{\rm main}$, where $Z_{\rm main}$ is the atomic charge of Beryllium (the main impurity). The total $W_{\rm th}$ is shown in figure 3(*a*) and it is rather constant within the error bars, in the range $W_{\rm th} = 2.9 - 3.1\,$MJ. Figure 3(*a*) shows also the pedestal stored energy $W_{\rm th}^{\rm ped}$ and the core stored energy $W_{\rm th}^{\rm core}$. The pedestal stored energy has been determined from the pedestal pressure as discussed in [35], while the core stored energy as $W_{\rm th}^{\rm core} = W_{\rm th} - W_{\rm th}^{\rm ped}$. The behaviour of the pedestal will be discussed in detail in section 5, but from figure 3(*a*) we can already note a change in the pedestal, with $W_{\rm th}^{\rm ped}$ that increases from $\approx 0.7\,$MJ in deuterium to $\approx 1.0\,$MJ in tritium. The core stored energy has a weak reduction from $\approx 2.3\,$MJ in deuterium to $\approx 2.1\,$MJ in tritium. It is not shown here, but the fast particle stored energy $W_{\rm f}$ (determined with TRANSP [52, 53]) also varies in the $A_{\rm eff}$ scan dataset from $\approx 0.3\,$MJ in deuterium to $\approx 0.2\,$MJ in tritium. So, $\beta_{\rm N}$ in the $A_{\rm eff}$ scan dataset remains around 1.5 because the increase in $W_{\rm th}^{\rm ped}$ with increasing $A_{\rm eff}$ is compensated by a reduction in both $W_{\rm th}^{\rm core}$ and $W_{\rm f}$.

The loss power has been determined as $P_{\rm loss} = P_{\rm abs} - \langle {\rm d}W/{\rm d}t\rangle$, where $\langle {\rm d}W/{\rm d}t\rangle$ is the time derivative of the total stored energy averaged over a time interval longer than the ELM cycle. The term $\langle {\rm d}W/{\rm d}t\rangle$ is negligible in steady state, so $P_{\rm loss} \approx P_{\rm abs}$ (with $P_{\rm abs}$ shown in figure 1).

The corresponding energy confinement time is shown in figure 3(*b*), where a clear positive correlation between $\tau_{\rm E}^{\rm th}$ and $A_{\rm eff}$ can be seen. The result has been strengthened by adding in figure 3(*b*) the thermal energy confinement determined by TRANSP (black empty triangles). A good agreement can be seen. Note that also the D pulse #96418 (blue asterisk, characterized by the same $P_{\rm sep}$ as the T pulse #100247) has $\tau_{\rm E}^{\rm th}$ lower than the T pulse #100247. This shows that the difference in the energy confinement in the $A_{\rm eff}$ scan dataset is not due the change in $P_{\rm sep}$ but it is in large part linked to the effect of the isotope mass.

The positive correlation observed in figure 3(*b*) is in qualitative agreement with the recent JET-ILW results in hydrogen and deuterium described in [11, 25] where $\tau_{\rm E}^{\rm th} \propto A^{0.4}$ was obtained. The trend $A^{0.4}$ is qualitatively shown in figure 3(*b*) with a dashed line. However, we can note that $\tau_{\rm E}^{\rm th}$ of the T pulse is higher than the $A^{0.4}$ trend. This is due to the power dependence of the energy confinement time which, according to the $H_{98(y,2)}$ scaling [21], is $\tau_{\rm E}^{\rm th} \propto P^{-0.69}$ and to the fact that the T pulse has lower power than the D pulses. Once the $H_{98(y,2)}$ power dependence has been removed for the entire dataset, a very good agreement with the $A^{0.4}$ trend is obtained, as shown in figure 3(*c*). Since the present dataset does not contain enough data points to reach a robust scaling of the energy confinement time with the isotope mass, no regression analysis has been attempted. For reference, $H_{98(y,2)}$ is of the order of 0.80.

Preliminary analysis with TRANSP using the experimental profiles of the toroidal velocity suggests also an increase in the momentum confinement time, from $\tau_{\rm M} \approx 0.15\,$s for the D pulse #96208 to $\tau_{\rm M} \approx 0.4\,$s for the T pulse #100247. However, a detailed study on momentum confinement time and momentum transport is outside the scope of this work and it is kept for a future investigation.

4.2. Power through the separatrix

The power through the separatrix has been determined as:

$$P_{\rm sep} = P_{\rm abs} - \langle {\rm d}W/{\rm d}t\rangle - P_{\rm rad,bulk}. \quad (2)$$

As described above, $\langle {\rm d}W/{\rm d}t\rangle$ is negligible in the steady phases. $P_{\rm rad,bulk}$ is the total radiated power inside the separatrix and has been determined from tomographic reconstructions

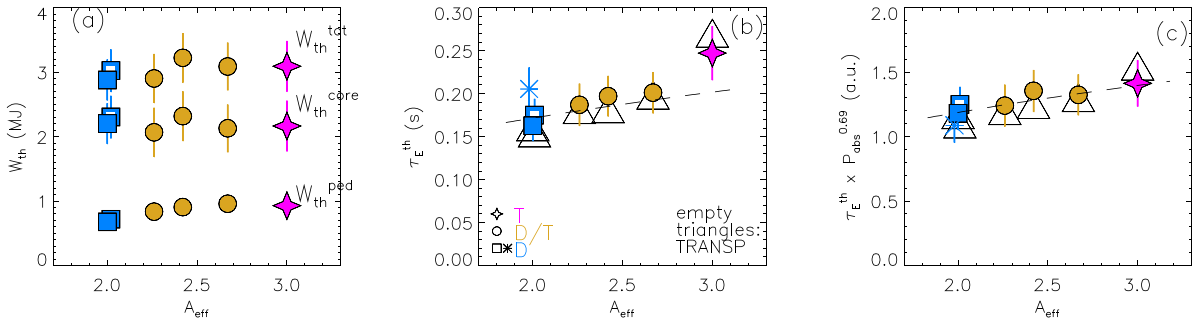

Figure 3. (*a*) Thermal stored energy versus $A_{\rm eff}$. The top row of data shows the total thermal stored energy, the middle row shows the core thermal stored energy and the bottom row the pedestal thermal stored energy. (*b*) Thermal energy confinement versus $A_{\rm eff}$. (*c*) Thermal energy confinement with the $H_{98(y,2)}$ power dependence removed versus $A_{\rm eff}$. The full symbols represent the thermal energy confinement determined by volume integrating the kinetic profiles and the empty triangles represents the TRANSP results. The dashed line represent the scaling $\tau_e^{\rm th} \propto A^{0.4}$.

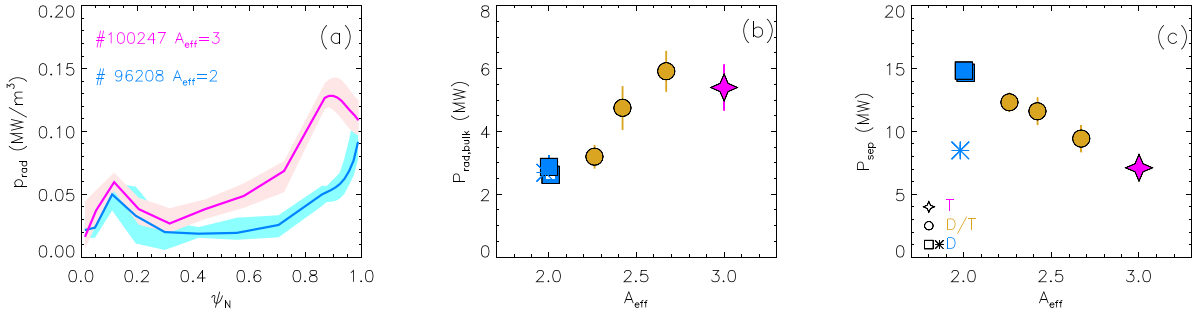

Figure 4. (*a*) Poloidally averaged radiated power profile in the pre-ELM phase for the D pulse #96208 and the T pulse #100247. The thick lines represent $P_{\rm rad}$ averaged over ten different pre-ELM phases while the shaded areas highlight the range of variation of $P_{\rm rad}$. (*b*) Power radiated from the bulk plasma and (*c*) power through the separatrix versus $A_{\rm eff}$.

in pre-ELM time windows. The poloidally averaged radiated power profiles in the pre-ELM phase determined via the tomographic reconstruction of multi-chord bolometry data for the D pulse #96208 and the T pulse #100247 are shown in figure 4(*a*). The T pulse has clearly higher radiated power than the D pulse. The volume integrated power radiated by the bulk plasma, $P_{\rm rad,bulk}$, is shown in figure 4(*b*). $P_{\rm rad,bulk}$ has a clear increase with increasing $A_{\rm eff}$, with a saturation above $A_{\rm eff} > 2.7$. The concentrations of nickel, iron and copper do not change significantly in the $A_{\rm eff}$ scan dataset but, unfortunately, measurements of tungsten concentration are not available as the diagnostic was not compatible with T operation. While the reason for the $P_{\rm rad,bulk}$ increase is still unclear, we speculate it might be due to a higher tungsten impurity sputtering yield by T than by D ions. $P_{\rm sep}$ is shown in figure 4(*c*). A clear reduction of $P_{\rm sep}$ with increasing $A_{\rm eff}$ can be seen, with $P_{\rm sep} \approx 15$ MW for the two D pulses and $P_{\rm sep} \approx 8$ MW for the T pulse. As described in section 3, the D pulse #96418 (blue asterisk) has been selected to have $P_{\rm sep}$ as close as possible to the T pulse #100247 (magenta star). As shown in figure 4(*c*), #96418 has $P_{\rm sep} \approx 8$ MW and #100247 has $P_{\rm sep} \approx 7.5$ MW.

4.3. ELM frequency and ELM type

The ELM frequency $f_{\rm ELM}$ versus $P_{\rm sep}$ is shown in figure 5 for the $A_{\rm eff}$ scan dataset and for the extended dataset. $f_{\rm ELM}$ has a clear positive dependence on $P_{\rm sep}$, with an increase from $\approx 5-10$ Hz at $P_{\rm sep} \approx 5$ MW to 100 Hz at $P_{\rm sep} \approx 15$ MW. Considering only the $A_{\rm eff}$ scan dataset, figure 5 could be misleading, suggesting that T plasmas are characterized by a significantly lower $f_{\rm ELM}$ ($\approx 5-20$ Hz) than D plasmas (≈ 100 Hz). However, in large part this difference is due to the different power necessary to keep $\beta_N \approx 1.5$. By looking at the extended dataset, it is clear that the D plasmas can reach $f_{\rm ELM} \approx 20$ Hz at low power. For the same $P_{\rm sep}$ no systematic difference in $f_{\rm ELM}$ can be seen between D plasmas and T plasmas. Note that the gas rate is different between the extended dataset and the $A_{\rm eff}$ scan dataset, as shown in figure 1(*a*). So this analysis cannot exclude a difference in $f_{\rm ELM}$ between D and T plasmas at constant gas rate.

The clear positive correlation between $f_{\rm ELM}$ and $P_{\rm sep}$ shown in figure 12 strongly suggests that the plasmas analysed in this work are characterized by type I ELMs. Ideally, a power scan at constant gas rate for each $A_{\rm eff}$ data point would be necessary for a more firm conclusion. This can be done for the D pulses, where the blue asterisk and the blue full squares have similar gas rate but different $P_{\rm sep}$. Moreover, the deuterium subset is part of a wider deuterium dataset that was clearly identified as type I ELMy H-modes [36]. Unfortunately, a power scan at constant gas rate was not possible for the T pulse and the D/T pulses due to the strict limits in the gas consumption and in the neutron budget. However, the T pulse has a very low $f_{\rm ELM}$ which makes it compatible with type I ELMs. Finally,

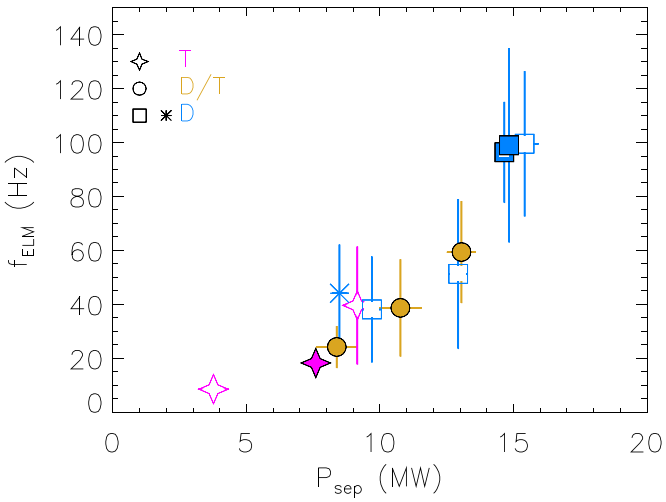

Figure 5. ELM frequency versus power through the separatrix for the $A_{\rm eff}$ scan dataset (full symbols with black outline) and for the extended dataset (empty symbols).

as discussed later in figure 14(*c*), the ELM energy losses are rather large and consistent with those of type I ELMs.

Therefore, we can conclude that the pulses discussed in this work are type I ELMy H-modes.

5. Variation of the pedestal structure with A_{eff}

The pre-ELM density profiles and the corresponding fits for the D pulse #96208, the D/T pulse #99480 and the T pulse #100247 are shown in figure 6(*a*). As the T content in the plasma increases in the scan, the pedestal top density increases. In the SOL, no significant difference is present within the scatter of the data. The pre-ELM temperature profiles are shown in figure 6(*b*). $T_{\rm e}^{\rm ped}$ is lower in the T plasma than in the D plasma. However, we remind that the T plasma has lower power than the D plasma to keep $\beta_{\rm N} \approx 1.5$ ($T_{\rm e}^{\rm ped}$ does not change at constant power, as discussed in [54]). Finally, the pre-ELM pressure profiles are shown in figure 6(*c*). Due to the large increase in $n_{\rm e}^{\rm ped}$ from the D pulse to the T pulse, the pedestal pressure is higher in the T pulse than in the D pulse, despite the lower $T_{\rm e}^{\rm ped}$.

To quantify the results shown in the profiles of figure 6, information on pedestal height, width, and position have been systematically extracted from the fitting parameters. Figure 7 shows the pedestal height versus $A_{\rm eff}$. The pedestal height in figure 7 is the height parameter in the *mtanh* definition [47], which represents the height just below the pedestal knee. A different definition, using the value of the experimental data just above the pedestal knee (for example at $\psi_{\rm N} = 0.93$, see figure 6), leads to qualitative similar results. The pedestal density $n_{\rm e}^{\rm ped}$ increases systematically with increasing $A_{\rm eff}$, perhaps with a weak saturation above $A_{\rm eff} > 2.7$, see figure 7(*a*). The increase is $\approx 50\%$ from $n_{\rm e}^{\rm ped} = 4 \times 10^{19} {\rm m}^{-3}$ for the D plasmas to $n_{\rm e}^{\rm ped} = 6.2 \times 10^{19} {\rm m}^{-3}$ for the T plasma. This is qualitatively consistent with other recent results from type I ELMy H-modes from the D/T campaign [54]. $T_{\rm e}^{\rm ped}$ decreases with increasing $A_{\rm eff}$, figure 7(*b*), with a $\approx 25\%$ decrease from the D plasmas to the T plasmas. As a result of the stronger $n_{\rm e}^{\rm ped}$ increase, the pedestal pressure also increases with $A_{\rm eff}$, as shown in figure 7(*c*). Note the trends of figure 7 are still present (albeit a bit weaker) when comparing the D pulse and the T pulse with similar $P_{\rm sep}$, #96418 (blue asterisk) and #100247 (magenta star).

The pedestal widths of the density, temperature and pressure profiles are shown in figure 8. The density width $w_{\rm ne}$ is shown in figure 8(*a*), where a weak increase from D to T can be observed. Overall, within the uncertainties, the pedestal width of temperature and pressure do not vary with $A_{\rm eff}$, as shown in figures 8(*b*) and (*c*). This result is consistent with that obtained with a $A_{\rm eff}$ scan dataset at constant power and constant gas rate discussed in [54]. Note that in figure 8(*c*) the pressure width has been determined by fitting the experimental pressure pre-ELM data. It is common also to define the pressure width as $w_{\rm pe} = (w_{\rm Te} + w_{\rm ne})/2$. The use of this definition would not lead to any significant difference in this dataset. For completeness, the correlation between the pressure width and the poloidal beta at the pedestal top ($\beta_\theta^{\rm ped}$) is shown in figure 9. The dashed lines show the relation $w_{\rm pe} = k(\beta_\theta^{\rm ped})^{0.5}$. The standard EPED1 relation assumes $k = 0.076$ [55]. The experimental width is approximately 30%–40% higher than the EPED1 expectations and is closer to $k = 0.1 - 0.11$. As discussed in the last section, this result suggests that the present predictive pedestal models are not ready yet to reliably predict the pedestal in D/T and T plasma.

Since the pedestal width does not change significantly with $A_{\rm eff}$, the variation in the pedestal height is mainly driven by the pedestal gradients. This is shown in figure 10. The pre-ELM pedestal gradients have been calculated in the normalized poloidal flux and they represent the average gradient in the pedestal region. The maximum gradients have similar qualitative trends and will be shown in section 10 when discussing the pedestal stability. The pedestal density gradient is shown in figure 10(*a*). A 50% increase from $\langle \nabla n_{\rm e}^{\rm ped} \rangle \approx 60 \times 10^{19} {\rm m}^{-3}/\psi_{\rm N}$ in the D plasmas to $\langle \nabla n_{\rm e}^{\rm ped} \rangle \approx 90 \times 10^{19} {\rm m}^{-3}/\psi_{\rm N}$ in the T plasma can be observed. The temperature gradient decreases by 25% from $\langle \nabla T_{\rm e}^{\rm ped} \rangle \approx 8.5\ keV/\psi_{\rm N}$ in D to $\langle \nabla T_{\rm e}^{\rm ped} \rangle \approx 6.5\ keV/\psi_{\rm N}$ in T. As a result of the stronger $\langle \nabla n_{\rm e}^{\rm ped} \rangle$ increase, the pressure gradient increases by 25% from the D pulses to the T pulse. Similar qualitative trend can be observed when comparing the D pulse and the T pulse with similar $P_{\rm sep}$, #96418 (blue asterisk) and #100247 (magenta star).

The results of figure 10 show that the variations in the pre-ELM $n_{\rm e}^{\rm ped}$ and $T_{\rm e}^{\rm ped}$ are mainly due to a change in the gradients. This motivates the study of the inter-ELM pedestal transport discussed in section 7 and in section 9. Moreover, since the dataset has the same equilibrium, the increase of the pre-ELM $\langle \nabla p_{\rm e}^{\rm ped} \rangle$ with increasing $A_{\rm eff}$ shows that the pedestal stability improves with increasing T content. The pedestal stability will be discussed in section 10.

The ratio between separatrix density and pedestal density ($n_{\rm e}^{\rm sep}/n_{\rm e}^{\rm ped}$) and the pedestal position can have a significant effect on the pedestal stability [32–36, 51, 56]. Since the goal of the work is to assess the direct effect of the isotope mass on

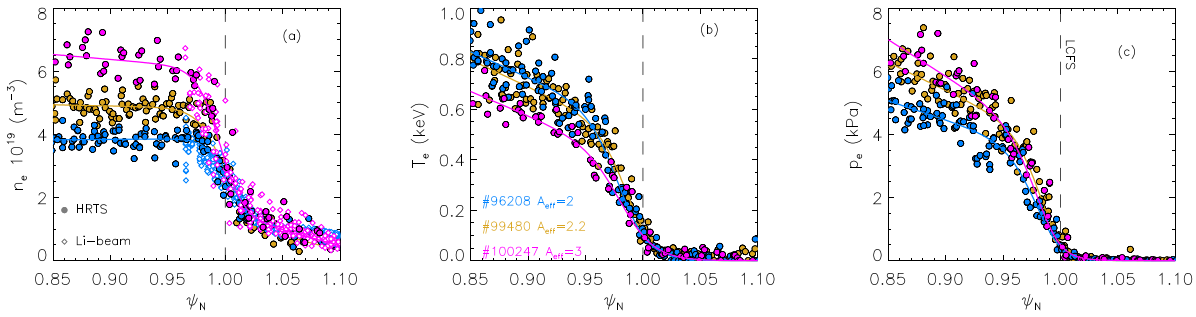

Figure 6. Pre-ELM profiles of electron density (*a*), temperature (*b*) and pressure (*c*) for the D pulse #96208 (blue), the D/T pulse 99480 (gold) and the T pulse #100247 (magenta) from HRTS (circles) and Li-beam (diamonds). The continuous lines show the fit to the experimental data.

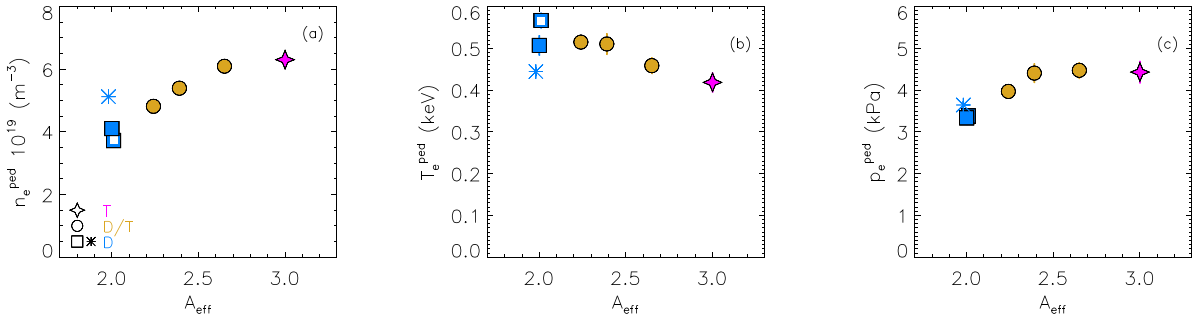

Figure 7. Dependence of the pedestal height of electron density (*a*), temperature (*b*) and pressure (*c*) on $A_{\rm eff}$.

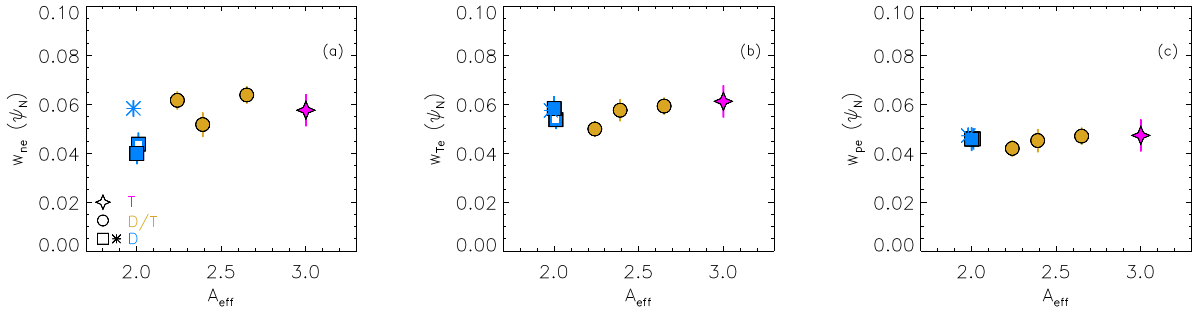

Figure 8. Correlation of the pedestal width of electron density (*a*), temperature (*b*) and pressure (*c*) with $A_{\rm eff}$. The width of the pressure has been determined from the fits to the experimental pressure data.

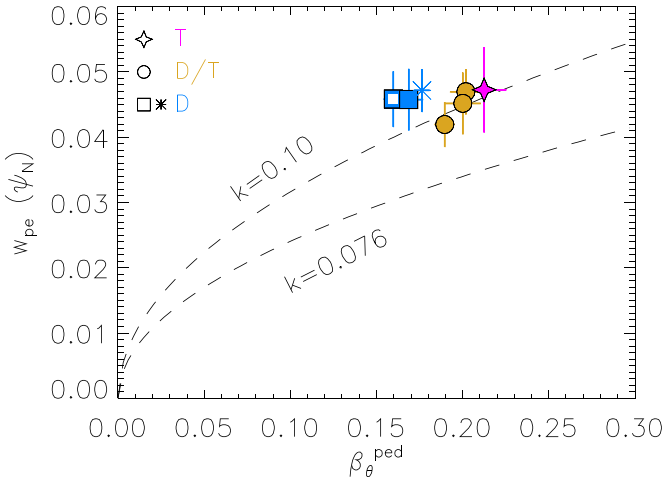

Figure 9. Correlation between pressure width and β poloidal at the pedestal top.

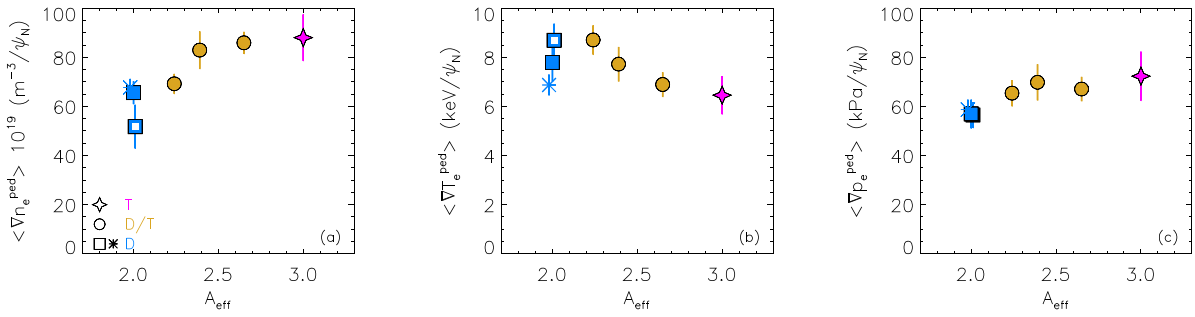

Figure 10. Correlation of the average pedestal gradients of electron density (*a*), temperature (*b*) and pressure (*c*) with $A_{\rm eff}$.

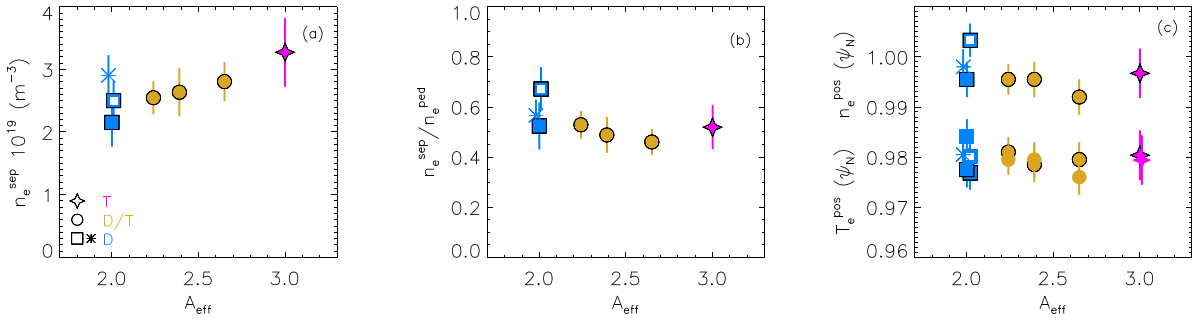

Figure 11. Dependence of the electron separatrix density (*a*), ratio $n_{\rm e}^{\rm sep}/n_{\rm e}^{\rm ped}$ (*b*) and pedestal positions (*c*) on $A_{\rm eff}$. The symbols without black outline in frame (*c*) represent the position of the pedestal pressure.

the pedestal, it is important to verify that these parameters do not change significantly in the dataset. Figure 11(*a*) shows the separatrix density and its dependence on $A_{\rm eff}$. $n_{\rm e}^{\rm sep}$ has been determined as the value of the fitted density at the separatrix (after the profiles have been shifted to have $T_{\rm e}^{\rm sep}$ from the two point model, see section 3). The error bars represent the standard deviation of the experimental data in a narrow region around the separatrix. $n_{\rm e}^{\rm sep}$ shows a clear increase with increasing $A_{\rm eff}$. The change in $n_{\rm e}^{\rm sep}$ can be due to a change in the particle transport (as suggested in [30]) and/or to a change in the source term from D to T (as suggested in [57]). However, since also $n_{\rm e}^{\rm ped}$ increases with increasing isotope mass, the ratio $n_{\rm e}^{\rm sep}/n_{\rm e}^{\rm ped}$ is approximately constant, as shown in figure 11(*b*). Only the D pulse #96208 shows a slightly higher $n_{\rm e}^{\rm sep}/n_{\rm e}^{\rm ped}$ than the rest of the dataset. This difference is rather small and cannot lead to any major change in the pedestal properties, as shown for JET-ILW deuterium plasmas in [36]. Finally, figure 11(*c*) shows the position of the pedestal density $n_{\rm e}^{\rm pos}$ and of the pedestal temperature $T_{\rm e}^{\rm pos}$, defined as the position of the maximum gradients of $n_{\rm e}$ and $T_{\rm e}$ respectively. $T_{\rm e}^{\rm pos}$ is rather constant at $\approx 0.98\,\psi_{\rm N}$ with no correlation with $A_{\rm eff}$. $n_{\rm e}^{\rm pos}$ is also rather constant at $\approx 0.995\,\psi_{\rm N}$. The D pulse #96208 has a slightly more outward density position, consistent with the fact that also $n_{\rm e}^{\rm sep}/n_{\rm e}^{\rm ped}$ is higher than the rest of the dataset. For completeness, figure 11(*c*) shows also the position of the pedestal pressure $p_{\rm e}^{\rm pos}$ using symbols with no outline. $p_{\rm e}^{\rm pos}$ is almost identical to $T_{\rm e}^{\rm pos}$ and shows no variation with $A_{\rm eff}$. Therefore, in this dataset the effect on the pedestal of the isotope mass is not due to an indirect effect related to variations in $n_{\rm e}^{\rm sep}/n_{\rm e}^{\rm ped}$, nor in the pedestal positions.

Finally, the toroidal velocity in the pedestal region is shown in figure 12. The measurements are done with charge exchange diagnostic using trace neon puffs and they correspond to the toroidal velocity of the neon. The pre-ELM profiles for the D pulse #96208, the D/T pulse #99480 and the T pulse #100247 are shown in figure 12(*a*). No significant difference can be seen, with velocity that is very similar in D and T both at the pedestal top and at the pedestal foot. Hence, the gradient of the toroidal velocity in the pedestal is not significantly different between the D pulse and the T pulse either. The toroidal velocity at the pedestal top is shown for the entire $A_{\rm eff}$ scan dataset in figure 12(*b*). For simplicity, the velocity at the pedestal $v_\phi{}^{\rm ped}$ is defined as the value at $\psi_{\rm N} = 0.9$. No systematic variation with $A_{\rm eff}$ can be observed and $v_\phi{}^{\rm ped}$ is in the range 10–12 krad s^{-1}. Since the rotation might have an effect on the pedestal stability, as shown in [10, 58, 59], this result suggests that the difference in the pedestal stability discussed in section 10 is not due to a difference in the toroidal velocity.

6. Variation of ELM losses with $A_{\rm eff}$

The first part of the section quantifies the ELM energy loss $W_{\rm ELM}$ and its variation in the isotope mass scan dataset. The second part of the section assesses if the variation of the ELM energy losses is due mainly to changes in the conductive or convective terms by looking at the $n_{\rm e}$ and $T_{\rm e}$ drops at the pedestal top.

6.1. ELM energy losses

The ELM energy losses have been determined with three approaches, first from the time evolution of the diamagnetic stored energy $W_{\rm dia}$ and of the plasma stored energy $W_{\rm p}$, then by

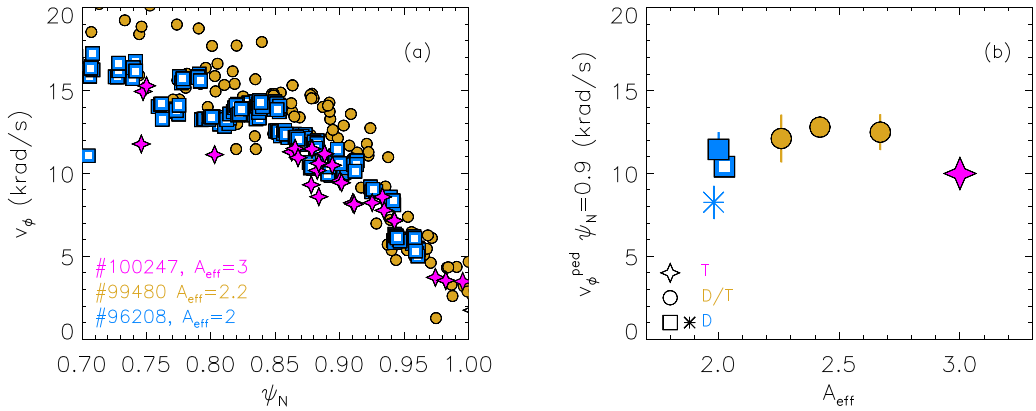

Figure 12. Pre-ELM profiles of the Neon toroidal velocity for the D pulse #96208 (blue) the D/T pulse #99480 (gold) and the T pulse #100247 (magenta) from CX (*a*). Toroidal velocity at $\psi_N = 0.9$ versus A_{eff} for the entire A_{eff} scan dataset.

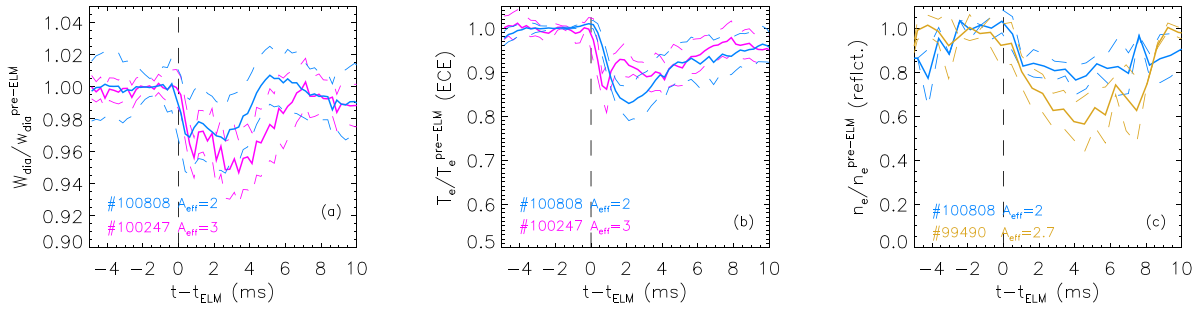

Figure 13. ELM synchronized time evolution of W_{dia} (*a*), electron temperature at the pedestal top from the ECE (*b*) and electron density at the pedestal top from reflectometry (*c*). The continuous lines show the average, while the dashed lines highlight the standard deviation. Data are normalized to their pre-ELM values.

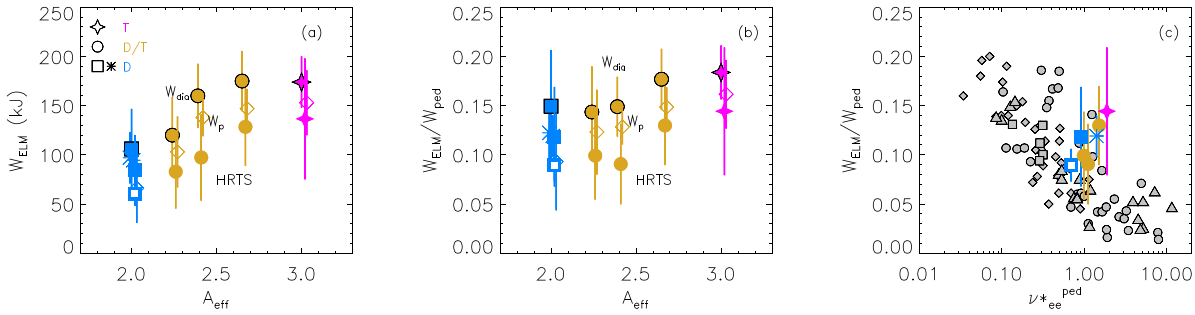

Figure 14. ELM energy losses (*a*) and normalized ELM energy losses (*b*) versus A_{eff}. The symbols with the black outline highlight data determined with W_{dia}, while the symbols with no outline those with HRTS. W_{ped} is determined from the HRTS. Frame (*c*) shows the correlation of the relative ELM energy losses with the pedestal collisionality. The grey symbols are the type I ELMs from the multi-machine analysis in [61].

volume integrating the pressure profile from fits to pre-ELM and post-ELM experimental HRTS data.

Figure 13(*a*) describes the first approach, using the W_{dia} time evolution. To calculate W_{ELM}, the W_{dia} signal has been ELM syncronyzed and its averaged time evolution has been determined for several ELMs selected during a steady phase of the pulse. Figure 13(*a*) shows with the continuous lines the average W_{dia} time evolution for the T pulse #100247 and for the D pulse #100808. The dashed lines represent the corresponding standard deviation. For a more clear comparison between the D and T pulses, the signal has been normalized to its pre-ELM value. The standard deviation is rather large, but the T plasma has slightly larger normalized ELM energy losses than the D plasma. W_{ELM} has been quantified as the difference between the pre-ELM W_{dia} and the W_{dia} minimum value after the ELM crash. The ELM energy losses determined for the A_{eff} scan dataset are shown in figure 14(*a*) using the symbols with a black outline. W_{ELM} increases from ≈ 110 kJ for the D plasmas to ≈ 180 kJ at $A_{eff} \approx 2.5$, while W_{ELM} tends to saturate at higher T content.

A similar analysis has been repeated using the plasma stored energy W_p. W_{ELM} determined with W_p is shown in figure 14(*a*) with empty diamonds. Qualitatively, the trend is similar to that obtained for W_{dia}, while quantitatively the W_p

ELM energy losses are only slightly lower than those determined with W_{dia}.

The third approach to estimate W_{ELM} has used the experimental density and temperature profiles from the HRTS. The method is described in detail in [60] and recently applied to assess the ELM losses in H and D plasmas in [26]. First, the pre-ELM and post-ELM n_e and T_e profiles have been determined in a steady phase of the pulse. The pre-ELM profiles have been defined as those located in the 70%–99% time window in the ELM cycle. The post-ELM profiles have been defined as those located in the 1%–10% time window in the ELM cycle. Then, the pressure profiles have been fitted and volume integrated obtaining the electron thermal stored energy (W_e^{th}) before and after the ELM. The ELM losses for the electron channel have been determined as the difference of W_e^{th} before and after the ELM. The total W_{ELM} has been determined assuming $T_i = T_e$ (the integration time of the CX diagnostic is not low enough to properly resolve the T_i ELM drop) and $n_i = n_e\left(Z_{main} + 1 - Z_{eff}\right)/Z_{main}$, where Z_{main} is the atomic charge of Beryllium (the main impurity) and Z_{eff} is a line averaged value of the effective charge. The corresponding ELM energy losses determined with this approach are shown in figure 14(*a*) with the symbols with no outline. From a qualitative point of view the result is consistent with W_{dia} and W_p. From the quantitative point of view, the ELM losses determined with the HRTS are lower than those determined with W_{dia}. This can be due to at least two factors. First of all, the time resolution of the HRTS is not high enough to the determine the maximum energy losses. Second, the assumption $T_i = T_e$ in the post-ELM phase might not be valid. However, within the uncertainties, the three approaches lead to consistent results.

Figure 14(*b*) shows the ELM energy losses normalized to the pedestal stored energy W_{ped}. Since W_{ped} increases with increasing A_{eff}, see figure 3(*a*), W_{ELM}/W_{ped} has only a weak increase with increasing A_{eff}. Within the error bars, the W_{ELM}/W_{ped} increase from the D plasma to the T plasma is almost negligible.

Note that the same qualitative conclusions are obtained when comparing the D and T pulses with similar P_{sep}, #96418 (blue asterisk) and #100247 (magenta star).

Figure 14(*c*) shows W_{ELM}/W_{ped} determined from the HRTS versus the pedestal collisionality. For comparison, the grey data in figure 14(*c*) show the ELM energy losses of type I ELMy H-modes from the multi-machine analysis presented in [61]. The ELM energy losses of the present dataset are roughly in the same range of the type I ELMs energy losses of [61]. This result strengthen the conclusion that the present dataset is characterized by type I ELMs. Note that the range of variation of the pedestal collisionality is very small in the present A_{eff} scan dataset, so no conclusion can be drawn from figure 14(*c*) on the correlation between W_{ELM}/W_{ped} and collisionality.

6.2. Drops of T_e^{ped} and n_e^{ped} during ELMs

Understanding the reason for the positive correlation between W_{ELM} and A_{eff} shown in figure 14(*a*) is possible only via non-linear MHD simulations. However, from the experimental point of view, we can contribute by investigating whether the increase of the ELM energy losses is due to the increase of the convective losses or of the conductive losses. These have been estimated by quantifying the T_e drops and n_e drops near the pedestal top during the ELM crash.

The drops of n_e and T_e during the ELMs have been determined with several diagnostics. An ELM synchronized approach has been used, as described in detail in [26, 60]. The HRTS diagnostic can determine both the n_e and T_e ELM drops. Since the HRTS time resolution is 20 Hz (so not optimal to quantify the ELM drops), also ECE and reflectometry have been used to strengthen the conclusion (their time resolution is 2.5 kHz and 400 Hz respectively, for the pulses used in this work).

In this work, we have defined the ELM drops $\Delta T_{e,ELM}$ and $\Delta n_{e,ELM}$ as the T_e and n_e reductions at a fixed radial position, $\psi_N = 0.97$ for the density and $\psi_N = 0.95$ for the temperature (which correspond to the position of the pedestal top of density and temperature respectively). This approach allows a simple systematic comparison between different diagnostics. The results are shown in figure 15. Figure 15(*a*) shows the temperature drops determined with the HRTS and with the ECE. Both diagnostics show a weak decrease of $\Delta T_{e,ELM}$ with increasing A_{eff}. The T_e drops normalized at the pre-ELM pedestal top value are shown in figure 15(*c*). No clear trend with A_{eff} is present. However, the errors bars are very large, especially for drops determined with the HRTS. The ECE allows a more precise estimate due to the higher time resolution. As an example, the ELM synchronized time evolution of the ECE is shown in figure 13(*b*) for the D pulse #100808 and the T pulse #100247.

The density drops $\Delta n_{e,ELM}$ and the relative density drops $\Delta n_{e,ELM}/n_e^{ped}$ are shown respectively in figures 15(*b*) and (*d*). The HRTS results have been complemented by those obtained from the high time resolution reflectometer. Unfortunately, the reflectometer could not reach the pedestal top in the T pulse (due to the injected microwaves being absorbed at the edge at the $2 \times f_{ce}$ harmonic), so the density drops from reflectometry are available only till $A_{eff} = 2.7$ for the D/T pulse #99490. The time evolution of the ELM synchronized density for the D pulse #100808 and the D/T pulse #99490 are shown in figure 13(*c*), suggesting higher density drops at higher A_{eff}. This is clear from figures 15(*b*) and (*d*), which show a clear increase of the density drops with increasing A_{eff}. HRTS results and reflectometry results are consistent.

The same qualitative conclusions from figures 14 and 15 can be obtained when comparing the D and T pulses with similar P_{sep}, #96418 (blue asterisk) and #100247 (magenta star). This shows that the change in the ELM losses are not due to the variation of P_{sep} but to the isotope mass.

The results of figures 14 and 15 show that the increase of W_{ELM} with increasing A_{eff} is due to an increase of the ELM density drops. So, the ELM becomes more convective with increasing isotope mass in this A_{eff} scan. More convective ELMs were also observed in a recent work comparing JET-ILW hydrogen and deuterium plasmas [26], however the difference was systematic and observed for both the hydrogen

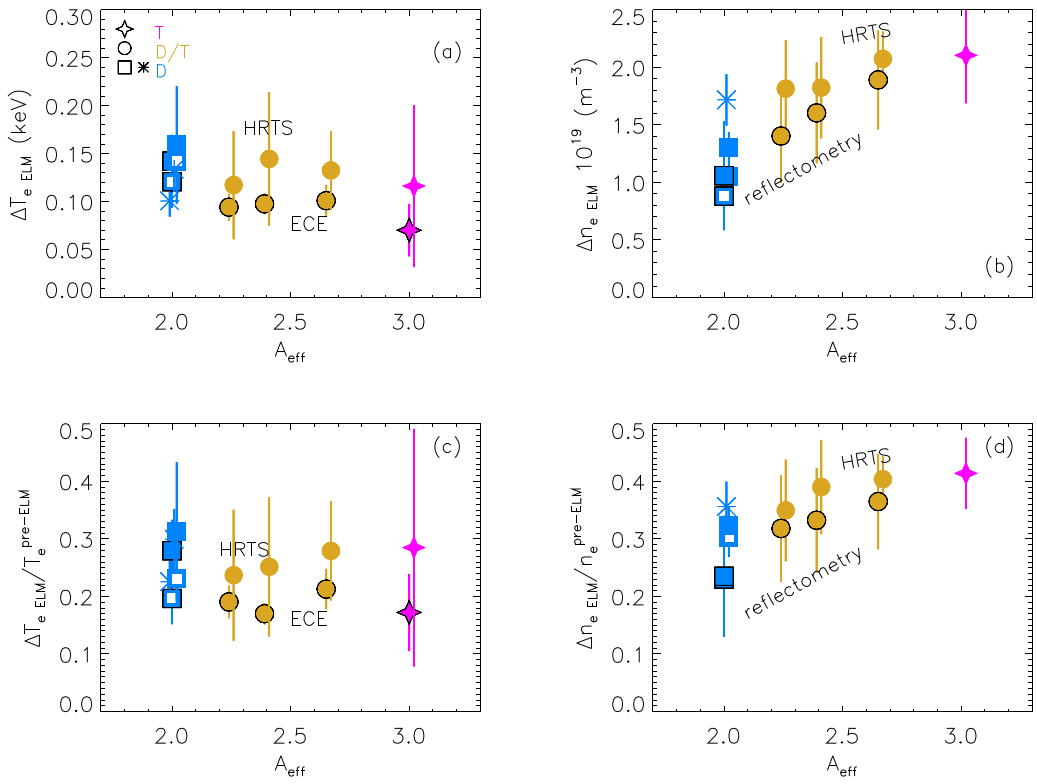

Figure 15. Drops in pedestal electron temperature (*a*) and density (*b*) at the ELM crash versus $A_{\rm eff}$. Frames (*c*) and (*d*) show the drops normalized at the pre-ELM values. The symbols with the black outline highlight data determined with ECE and reflectometry, while the symbols with no outline those with HRTS.

and the deuterium plasma, with no obvious difference related to the isotope mass.

7. Experimental results on the link between inter-ELM transport and A_{eff}

Reliable quantification of the inter-ELM pedestal transport is very challenging and not always possible. However, from an experimental point of view, it is possible to identify empirical inter-ELM pedestal parameters that can be indirectly linked to the transport. Section 7.1 describes the experimental results related to the heat transport. First, an empirical estimation of the heat diffusivity in the pedestal is shown. Then, this estimation is compared with more reliable results from TRANSP. Experimental analysis related to the inter-ELM particle transport is unfortunately not possible as discussed in section 7.2. Then, section 7.3 presents the behaviours of the gradient length of density and temperature in the pedestal, along with their ratio. The information of section 7.3 are strongly related to the electron-scale turbulent transport in the pedestal. Finally, section 7.4 presents an estimation of the parameter α_t that is related to the turbulent transport at the separatrix and in the SOL.

7.1. Inter-ELM heat transport in the pedestal

The results presented in section 5, and in particular in figure 10(*b*), show that the pedestal temperature gradient decreases with increasing $A_{\rm eff}$. This might lead to the misleading conclusion that the inter-ELM heat transport in the pedestal increases from D to T plasmas. Instead, this section shows that the change in $\nabla T_{\rm e}^{\rm ped}$ is mainly due to the reduction in the heat source from D to T (to keep similar $\beta_{\rm N}$). The results of this section also suggest a possible decrease of the pedestal inter-ELM heat transport with increasing $A_{\rm eff}$ however, due to the large uncertainties, no conclusive claims are possible.

As a first step, the variation of the pedestal electron heat diffusivity $\chi_{\rm e}$ in the $A_{\rm eff}$ scan dataset has been estimated from a qualitative point of view using basic experimental data. From the power balance, the radial profile of the electron heat diffusivity is:

$$\chi_{\rm e} = \frac{\int P_{\rm e} {\rm d}V}{S n_{\rm e} \nabla T_{\rm e}} \tag{3}$$

where $P_{\rm e}$ is the total heating to electrons, S is the area of the magnetic surface considered and $n_{\rm e}$ and $\nabla T_{\rm e}$ are the local electron density and electron temperature gradient respectively. The goal is to obtain only a basic experimental qualitative estimation of $\chi_{\rm e}$, so the inter-ELM electron heat diffusivity has been estimated from expression (3) using the following empirical expression:

$$\frac{P_{\rm sep} - P_{\rm ELM}}{2 S n_{\rm e}^{\rm ped} \langle \nabla T_{\rm e}^{\rm ped} \rangle} \tag{4}$$

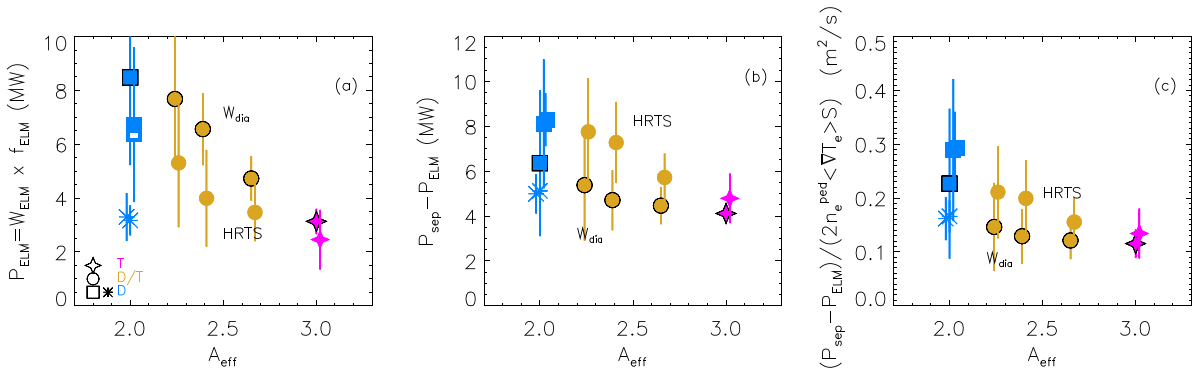

Figure 16. ELM power losses (a), power through the separatrix minus ELM power losses and data from expression (4) versus $A_{\rm eff}$. The symbols with the black outline highlight data determined with $W_{\rm dia}$, while the symbols with no outline those with HRTS.

where S is the plasma area at the LCFS, $n_{\rm e}^{\rm ped}$ is the pre-ELM pedestal density and $\langle\nabla T_{\rm e}^{\rm ped}\rangle$ is the pre-ELM average temperature gradient in the pedestal. The pedestal is rather close to the plasma edge so, for simplicity, no volume integration of the power density has been done, but the power through the separatrix is used. Since we are interested in the heat diffusivity before the ELM, in expression (4) the ELM power losses $P_{\rm ELM}$ have been subtracted [62]. The factor 2 in the denominator assumes that the power is equally distributed between electron and ions. This might overestimate the contribution from the total cross pedestal heat transport in the ion channel, which is usually less than that conducted by the electrons. $P_{\rm ELM}$ has been determined as $W_{\rm ELM}\times f_{\rm ELM}$ which, in a steady time interval, corresponds to the inter-ELM $\mathrm{d}W/\mathrm{d}t$. $P_{\rm ELM}$ for the $A_{\rm eff}$ scan dataset is shown in figure 16(a). $P_{\rm ELM}$ has been estimated using $W_{\rm ELM}$ from both $W_{\rm dia}$ and from the volume integration of the HRTS profiles, see figure 14(a). Both methods show a decreasing $P_{\rm ELM}$ with increasing $A_{\rm eff}$. The correlation is opposite to that of $W_{\rm ELM}$ with $A_{\rm eff}$ because in this dataset the ELM frequency decreases significantly with increasing $A_{\rm eff}$ (figure 5). $P_{\rm sep}-P_{\rm ELM}$ is shown in figure 16(b), where a decrease with increasing $A_{\rm eff}$ can be seen. Finally, the $\chi_{\rm e}$ proxy from expression (4) is shown in figure 16(c). The result suggests a negative correlation between the proxy and $A_{\rm eff}$. Unfortunately, the large error bars in the D plasmas in figure 16(c) (due to the large uncertainty in $P_{\rm ELM}$) do not allow any strong conclusion. Moreover, the D and T pulses with similar $P_{\rm sep}$ (#96418, blue asterisk, versus #100247, magenta star) have only marginally different $\chi_{\rm e}$ proxy. While figure 16(c) cannot prove a reduction of the pedestal inter-ELM heat transport with increasing isotope mass, at least it conclusively shows that the inter-ELM heat transport does not increase from the D plasmas to the T plasmas. So, the decreasing $\langle\nabla T_{\rm e}^{\rm ped}\rangle$ shown in figure 10(b) is clearly not due to an increasing inter-ELM heat transport with increasing $A_{\rm eff}$ but it is due to the decreasing $P_{\rm sep}-P_{\rm ELM}$ and increasing $n_{\rm e}^{\rm ped}$.

To strengthen this result, the heat diffusivity has been estimated also with TRANSP. TRANSP has used as inputs the fits to the experimental pre-ELM $T_{\rm e}$, $n_{\rm e}$ and $T_{\rm i}$ shown in figure 6 and the same improved EFIT++ equilibrium used throughout this work. Moreover, tomographic reconstructions done in the pre-ELM phase have been used for the radiated power. Then, TRANSP has calculated the effective heat diffusivity using the corresponding version of expression (3). The NBI and ICRH heating have been calculated with NUBEAM and TORIC [63, 64]. Figure 17(a) shows the volume integrated power deposition for the T pulse #100247 and the D pulse #96208. The thick line shows the total heating of electrons $P_{\rm e}$, while the thin line the total heating of ions $P_{\rm i}$. The dashed lines show the profiles of the radiated power $P_{\rm rad}$. Both $P_{\rm e}$ and $P_{\rm i}$ are lower in the T pulse (magenta lines) than in the D pulse (blue lines), consistent with the lower input power in T to maintain $\beta_{\rm N}\approx 1.5$. The dashed-dotted lines in figure 17(a) show the volume integrated $P_{\rm ELM}$ profile which is localized in the pedestal region. As also shown in figure 16(a), $P_{\rm ELM}$ is significantly higher in the D pulse than in the T pulse.

The effective heat diffusivity $\chi_{\rm eff}$ is shown in figure 17(b). The effective heat diffusivity is defined as $\chi_{\rm eff}=(q_{\rm e}+q_{\rm i})/(n_{\rm e}\nabla T_{\rm e}+n_{\rm i}\nabla T_{\rm i})$, where $q_{\rm e,i}$ is the electron/ion heat flux. Due to the fact that $T_{\rm i}=T_{\rm e}$ at the pedestal top, the electron-ion equipartition term is zero so it is not possible to separate $\chi_{\rm e}$ from $\chi_{\rm i}$ and only $\chi_{\rm eff}$ is shown in figure 17(b). Note that in the $(q_{\rm e}+q_{\rm i})$ calculation, the ELM power losses have been included by subtracting the $P_{\rm ELM}$ profiles. To assess the effect of the $T_{\rm i}^{\rm sep}$ uncertainty on $\chi_{\rm eff}$, the TRANSP runs have been done first assuming $T_{\rm i}^{\rm sep}=T_{\rm e}^{\rm sep}$ and then assuming $T_{\rm i}^{\rm sep}=400\,$eV as upper bound. The thick lines in figure 17(b) show the average diffusivity determined using the two assumptions. The shaded areas in figure 17(b) show the range of variation of the diffusivity. The range of variation is dominated by the uncertainty in $P_{\rm ELM}$ (see figure 16(a)), while the variation due to the $T_{\rm i}^{\rm sep}$ assumptions is rather small. $\chi_{\rm eff}$ is lower for the tritium pulse but unfortunately, due to the large uncertainty, no conclusive claims are possible. The result is consistent with the conclusion of figure 16. For reference, the dashed lines in figure 17(b) show $\chi_{\rm eff}$ determined without removing the ELM power losses. In this case the difference between the D pulse and the T pulses are significantly larger showing that the ELM power losses cannot be neglected in the $\chi_{\rm eff}$ calculation.

As a final comment, the neoclassical inter-ELM heat flux through the pedestal determined with the NEO code is small for the entire $A_{\rm eff}$ scan dataset, around 1 MW. This further motivates the investigation of the possible role of turbulent

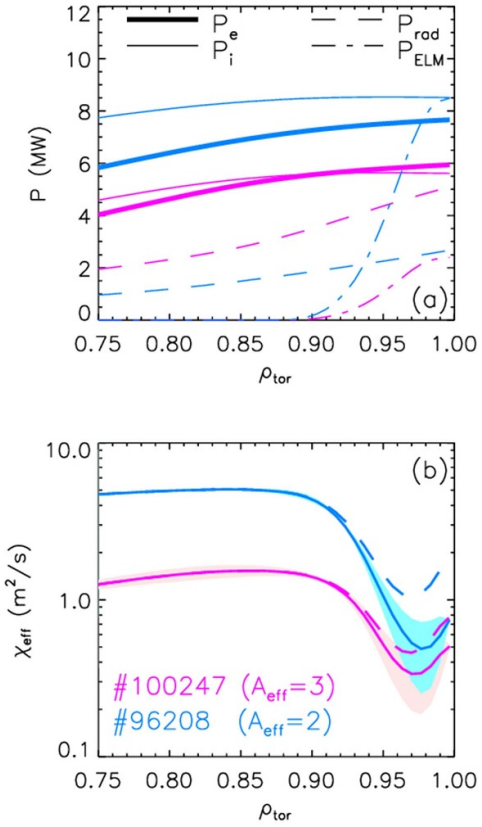

Figure 17. TRANSP results for the D pulse #96208 (blue) and the T pulses #100247 (magenta). Frame (*a*) shows the radial profile of the volume integrated power to electron (thick line), ion (thin line), radiated power (dashed) and ELM power losses. Frame (*b*) shows the radial profiles of the effective heat diffusivity. The thick lines in frame (*c*) show the average $\chi_{\rm eff}$ with $P_{\rm ELM}$ removed, while the dashed lines show $\chi_{\rm eff}$ without considering $P_{\rm ELM}$. The shaded areas in frame (*b*) highlight the $\chi_{\rm eff}$ range of variation (which is mainly due to the uncertainty in $P_{\rm ELM}$).

transport by studying the η parameter in section 7.3 and the pedestal microinstabilities in section 9.

The result of this section shows that the decrease of $\nabla T_{\rm e}^{\rm ped}$ with increasing $A_{\rm eff}$ observed in the present dataset is not due to an increase in the heat transport but it is due to the decrease of the heat source and the increase of $n_{\rm e}^{\rm ped}$ from the D to the T plasma. While experimental data might suggest a decrease of the pedestal inter-ELM heat transport with increasing $A_{\rm eff}$, no conclusive claims are possible due to the large uncertainties.

7.2. Inter-ELM particle transport in the pedestal

Assessing the experimental inter-ELM particle transport is more challenging than for the heat transport and not possible in this work due to the lack of a reliable quantification of the particle sources. Unfortunately, a reasonable quantification of the particle source using the emitted D_α radiation by the main chamber plasma is not possible due to the fact that the signal is dominated by the light emitted from the divertor region and reflected by the metallic walls. A recent attempt to remove the reflected light is described in [65] showing the estimates of the particle source are characterized by very high uncertainties. As shown in [65], due to these high uncertainties no univocal quantification of the inter-ELM particle diffusivity was possible even by constraining EDGE2D-EIRENE simulations with the experimental results. Moreover, due to the high $f_{\rm ELM}$, the inter-ELM phase of the low $A_{\rm eff}$ pulses are short and hence dominated by a post-ELM fast recovery. Experimental evidence suggests that this fast recovery may be driven by an increased recycling flux as a result of the increased particle flux arriving to the divertor targets and limiters during the ELM crash [65, 66].

To further complicate the experimental estimation of the inter-ELM particle transport, we cannot exclude a difference in the source term between D and T plasmas, as for example suggested in a recent SOLPS-ITER simulations in D/T plasmas [57].

7.3. Gradient length of density and temperate in the pedestal and $\eta_{\rm e}$

Here, we present the experimental characterization of the normalized gradient lengths that, from a theoretical point of view, are strongly linked to the turbulent transport. In this work we focus on three parameters, the normalized electron density gradient length, $R/L_{ne} = R\nabla n_{\rm e}/n_{\rm e}$, the normalized electron temperature gradient length, $R/L_{Te} = R\nabla T_{\rm e}/T_{\rm e}$, and their ratio $\eta_{\rm e} = L_{ne}/L_{Te}$. The increase of $\eta_{\rm e}$ tends to increase the $\rho_{\rm e}$-scale turbulent transport, as recently studied in the JET-ILW pedestal [30, 67, 68]. Due to the uncertainty in $T_{\rm i}^{\rm sep}$, an experimental estimation of $\eta_{\rm i}$is not possible.

The parameter $\eta_{\rm e}$ is the ratio between two gradients, so its uncertainty can be large. For this reason, $\eta_{\rm e}$ has been estimated with two complementary approaches. First using the fits to the experimental data, then using directly the experimental data of $T_{\rm e}$ and $n_{\rm e}$ from the HRTS.

The first row of figure 18 shows in frames (*a*), (*b*) and (*c*) the profiles of $\nabla n_{\rm e}/n_{\rm e}$, $\nabla T_{\rm e}/T_{\rm e}$ and $\eta_{\rm e}$ respectively, determined from the fits to the experimental data for the D pulse #96208, the D/T pulse #99491 and the T pulse #100247. The uncertainty has been determined as reliably as possible using the following approach. First, the experimental $n_{\rm e}$ and $T_{\rm e}$ profiles have been fitted with a *mtanh* function, obtaining the fitting parameters and their corresponding standard deviations. Then, using the mtanh function, many different profiles have been created using a Gaussian distribution of the fitting parameters. For each parameter, the Gaussian distribution has a standard deviation corresponding to the standard deviation of the parameter. Then, $\nabla n_{\rm e}/n_{\rm e}$, $\nabla T_{\rm e}/T_{\rm e}$ and $\eta_{\rm e}$ have been determined for each new profile. The shaded areas in the first row of figure 18 show the uncertainty determined as the standard deviation of the collected profiles. The thick lines in the first row of figure 18 show the average profiles determined as the average of the collected profiles.

By looking at the first row of figure 18, we can already reach two conclusions. First of all, $\nabla T_{\rm e}/T_{\rm e}$ does not change

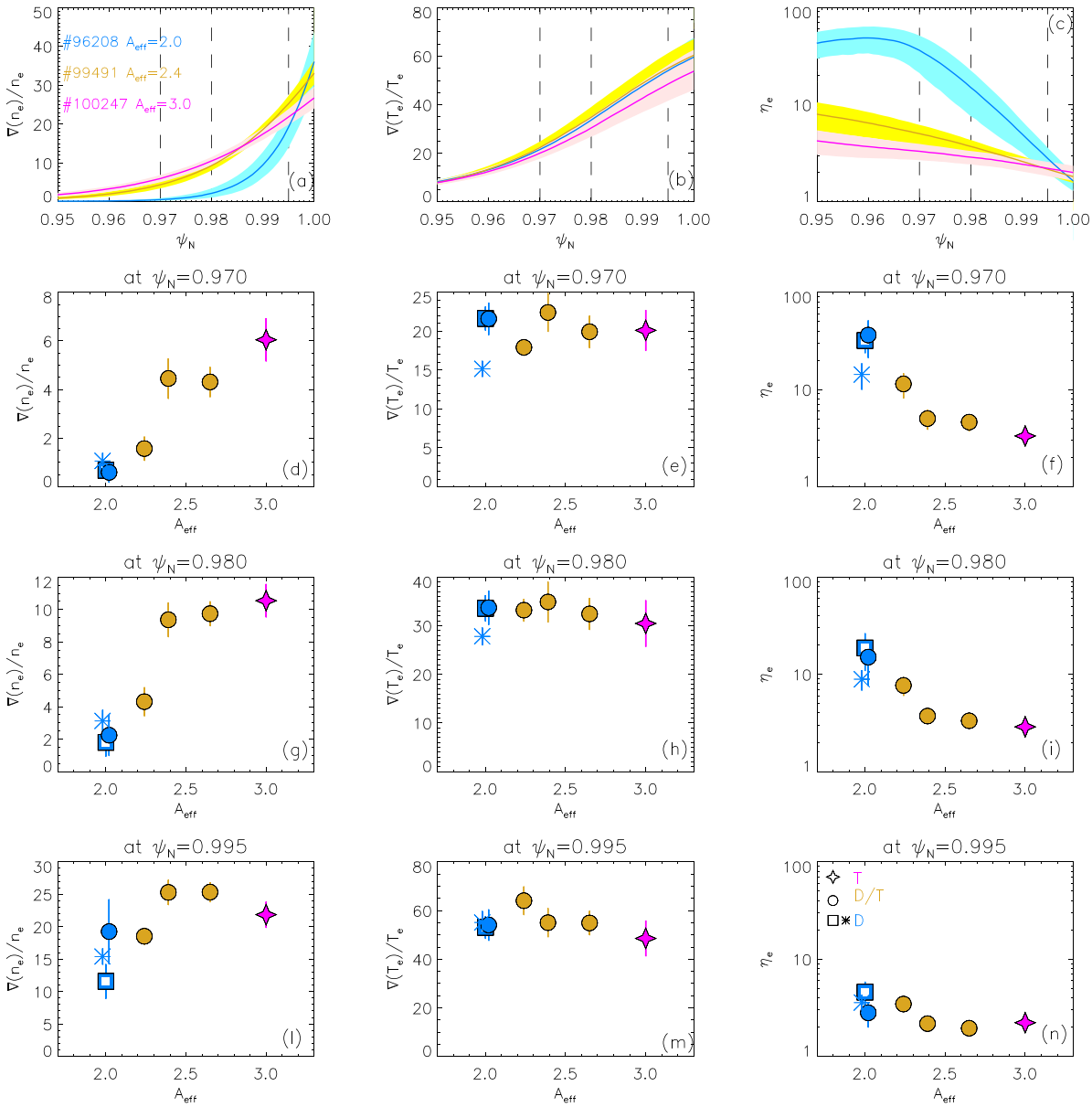

Figure 18. Profiles of the inverse gradient length of (*a*) density and (*b*) temperature and profile of η_e for the D pulse #96208 (blue), the D/T pulse #99491 (gold) and the T pulse #100247 (magenta). The following rows show the correlation with $A_{\rm eff}$ of the quantities determined near the pedestal top (at $\psi_{\rm N} = 0.97$, second row) near the position of the maximum temperature gradient (at $\psi_{\rm N} = 0.98$, third row) and near the position of the maximum density gradient (at $\psi_{\rm N} = 0.995$, fourth row).

significantly from the D pulse to the T pulse. Second, it is clear that $\eta_{\rm e}$ in the region $\psi_{\rm N} < 0.99$ is higher in the D pulse than in the T pulse. The behaviour of $\nabla n_{\rm e}/n_{\rm e}$ is more complex and conclusions depend on the radial position. The second row in figure 18 shows the values of $\nabla n_{\rm e}/n_{\rm e}$, $\nabla T_{\rm e}/T_{\rm e}$ and $\eta_{\rm e}$ for the entire $A_{\rm eff}$ scan dataset determined at $\psi_{\rm N} = 0.97$, approximately at the pedestal top of the density.$\nabla n_{\rm e}/n_{\rm e}$ shows a clear increase with increasing $A_{\rm eff}$, figure 18(*d*). As already mentioned $\nabla T_{\rm e}/T_{\rm e}$ is rather constant, figure 18(*e*), and $\eta_{\rm e}$ decreases with increasing $A_{\rm eff}$, figure 18(*f*). The third row in figure 18 shows the correlations determined at $\psi_{\rm N} = 0.98$. This location corresponds to the position of the maximum temperature gradient, as shown in figure 11(*c*). Approximately, the same behaviour described at $\psi_{\rm N} = 0.97$ can be seen. Finally, the third row in figure 18 shows the correlations determined at $\psi_{\rm N} = 0.995$, which corresponds to the position of the maximum density gradient, see figure 11(*c*). At this location, the variation in $\nabla n_{\rm e}/n_{\rm e}$ is very weak and $\eta_{\rm e}$ does not show any strong correlation with $A_{\rm eff}$.

The second approach to estimate $\eta_{\rm e}$ is shown in figure 19 and exploits directly the experimental data. From its definition, $\eta_{\rm e}$ can be determined as $\eta_{\rm e} = {\rm d}\ln(T_{\rm e})/{\rm d}\ln(n_{\rm e})$, so from a linear fit to $\ln(T_{\rm e})$ versus $\ln(n_{\rm e})$. Figure 19(*a*) shows the experimental $\ln(T_{\rm e})$ versus $\ln(n_{\rm e})$ around the separatrix, in the region $\psi_{\rm N} = 0.98 - 1.01$ for the D pulse #96208, the D/T pulse #99491 and the T pulse #100247. The three slopes are rather similar and indeed the values of $\eta_{\rm e}$ are constant over the entire dataset, as shown in figure 19(*c*). This is consistent with

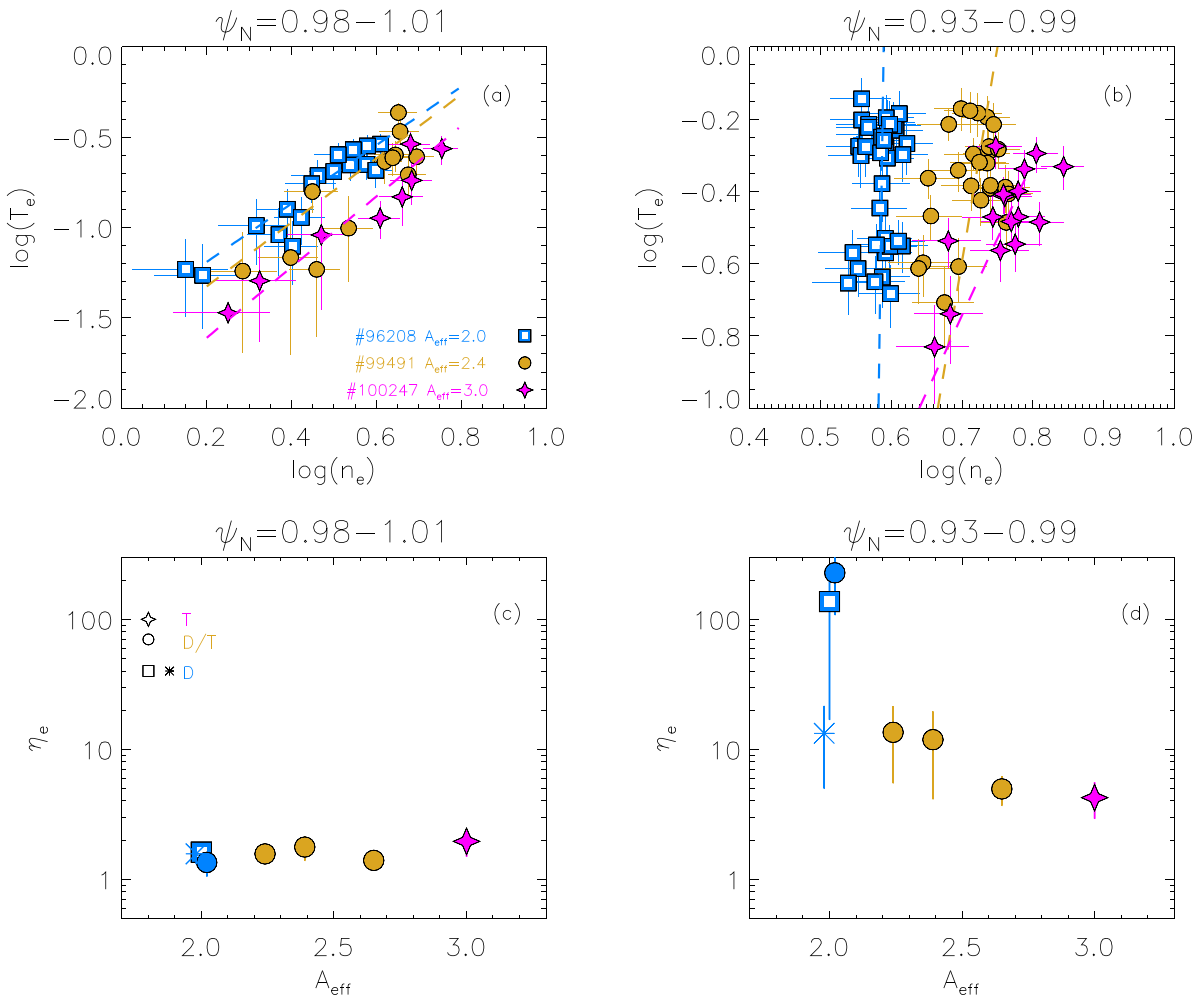

Figure 19. Logarithm of the temperature and density from the HRTS around the separatrix (a) and in the pedestal region (*b*). Frames (*c*) and (*d*) show the corresponding η_e determined from the linear fits to the data of frames (*a*) and (*b*).

the result shown in figure 18(*n*). Figure 19(*b*) shows the experimental $\ln(T_e)$ versus $\ln(n_e)$ chosen in a radial region that covers the whole pedestal, slightly inwards of the pedestal top to the pedestal foot. The slopes are clearly different and in particular the D pulse has almost a vertical slope. This leads to a significant variation of η_e with A_{eff}, as shown in figure 19(*d*). This is consistent with the results shown in figures 18(*f*) and (*i*).

Note that a recent JET-ILW analysis performed with pure D plasmas [62] has shown that η_e in the pedestal tends to increase with increasing P_{sep}. To test if the variation of η_e in figures 18 and 19 is due to a change in P_{sep} or in A_{eff} we can compare the D and T pulses with similar P_{sep}, #96418 (blue asterisk) and #100247 (magenta star). Both figures 18 and 19 show that η_e at the pedestal top is higher in the D pulse #96418 than in the T pulse #100247. The difference is however slightly weaker than for the A_{eff} scan dataset. This shows that the change in η_e in the A_{eff} scan dataset is due mainly to that the variation of isotopic composition, but also the variation of P_{sep} might play a role.

In conclusion, the present results show that at the pedestal top and in the middle of the pedestal η_e decreases with increasing A_{eff}, suggesting that the present dataset might be characterized by more ρ_e-scale turbulent transport in the D plasmas than in the T plasmas. The variation in η_e is driven by the variation of $\nabla n_e/n_e$, while $\nabla T_e/T_e$ is rather constant. At the pedestal foot, no strong correlation between η_e and A_{eff} has been found in the present dataset.

7.4. Experimental fingerprint of SOL turbulence

Concerning the SOL, direct measurements of the SOL turbulence are not available for this dataset. However, we can estimate the parameter α_t defined as:

$$\alpha_t \propto R q_{cyl}^2 \sqrt{\frac{m_e}{A_{eff}}} \frac{n_e^{sep}}{\left(T_e^{sep}\right)^2} Z_{eff}. \quad (5)$$

α_t is defined within the Drift-Alfvén turbulence (DALF) model [69–71]. From a physical point of view, it represents the ratio between two different turbulent transport mechanisms, the resistive ballooning versus the drift waves. Note an explicit $A_{eff}^{-0.5}$ dependence in the α_t definition, coming from an ion mass dependence appearing in the plasma resistivity (within

the DALF model normalizations). Due to the $A_{\rm eff}^{-0.5}$ dependence, the effective isotope mass can directly affect the level of resistive interchange turbulence at the separatrix.

In the α_t experimental estimation, the separatrix parameters have been evaluated at the radial position corresponding to $T_{\rm e} = T_{\rm e}^{\rm sep}$, where the separatrix temperature has been evaluated from the two point model. As discussed in section 3, $T_{\rm e}^{\rm sep}$ varies in the range 110–120 eV in the $A_{\rm eff}$ scan dataset. Overall, the α_t parameter does not seem to vary significantly, within the uncertainties. This is because the increase of $n_{\rm e}^{\rm sep}$ with $A_{\rm eff}$ shown in figure 10(*a*) is compensated by the term $A_{\rm eff}^{-0.5}$. The negligible variation of α_t suggests that the turbulence near the separatrix and in the SOL does not change significantly in the $A_{\rm eff}$ scan dataset. In absolute terms, $\alpha_t \leqslant 0.3$, within errorbars. According to [70], this might indicate that resistive ballooning turbulence is not affecting significantly the profiles nor the level of transport near the separatrix. This conclusion complements the result discussed in figure 19(*c*) in which it was shown that $\eta_{\rm e}$ was largely unvaried near the separatrix.

8. Link between $n_{\rm e}^{ped}$ and A_{eff}: role of ELM particle losses and pedestal density predictions

The discussion of the previous sections has shown that the major effect of $A_{\rm eff}$ occurs on the electron pedestal density, with a 50% increase in $n_{\rm e}^{\rm ped}$ from D to T. Gyro-kinetic simulations are on-going to study the origin of the $n_{\rm e}^{\rm ped}$ increase with $A_{\rm eff}$. In this section we investigate if the variation in $n_{\rm e}^{\rm ped}$ can be linked to the variation of the ELM particle losses from the D to the T plasmas. Then, we apply a recently developed density model to the $A_{\rm eff}$ scan dataset to further investigate possible mechanisms that might explain the $n_{\rm e}^{\rm ped}$ increase.

8.1. Pedestal density and rate of ELM particle losses

A possible mechanism that could explain the variation of the density with $A_{\rm eff}$ is a change of the particles lost during the ELMs. Assuming a similar source term and a similar particle transport, a plasma with higher ELM particle losses might have lower density [26]. Indeed, the pedestal density of the $A_{\rm eff}$ scan dataset decreases with increasing $f_{\rm ELM}$, as shown in figure 20(*a*) by the full symbols with black outline.

The total ELM particle losses during an ELM could be estimated by volume integrating the density profiles before and soon after an ELM. However, as discussed in section 7.2 and in [65], this value is likely affected by the strong recycling of the post-ELM phase, making this estimate very uncertain. For this reason we have used a simpler qualitative approach and the total particle losses are estimated using the density drop due to the ELM, $\Delta n_{\rm e}^{\rm ELM}$, determined from the HRTS diagnostic and discussed in figure 15(*b*). Assuming that the ELM affected region is not significantly different from pulse to pulse, $\Delta n_{\rm e}^{\rm ELM}$ is a reasonable qualitative estimate for the ELM particle losses. A similar investigation has been recently done for a set of JET-ILW hydrogen and deuterium plasmas, suggesting that the ELM particle losses might partially explain the lower density of the investigated H plasmas compared to the D plasmas [26].

The ELM density drop $\Delta n_{\rm e}^{\rm ELM}$ tends to increase from the D to the T plasma, as shown in section 6.2. However, the D pulses are characterized by significantly higher ELM frequency (figure 5) which compensates the lower $\Delta n_{\rm e}^{\rm ELM}$. The product $\Delta n_{\rm e}^{\rm ELM} \times f_{\rm ELM}$, representing an estimate of the ELM particle losses rate, is shown in figure 20(*b*). The $A_{\rm eff}$ scan dataset shows a clear reduction of $\Delta n_{\rm e}^{\rm ELM} \times f_{\rm ELM}$ with increasing $A_{\rm eff}$. Figure 20(*c*) shows the correlation between $\Delta n_{\rm e}^{\rm ELM} \times f_{\rm ELM}$ and $n_{\rm e}^{\rm ped}$. The negative correlation suggests that the increase of $n_{\rm e}^{\rm ped}$ with increasing $A_{\rm eff}$ might be due, at least in part, to the reduction of the ELM particle loss rate. To test this statement, the analysis has been repeated for the extended dataset discussed in section 2. The results are shown in figure 20 with the empty symbols. The extended dataset breaks the correlations of $\Delta n_{\rm e}^{\rm ELM} \times f_{\rm ELM}$ with $n_{\rm e}^{\rm ped}$. In particular, figure 20(*c*) shows that D and T pedestals with comparable $\Delta n_{\rm e}^{\rm ELM} \times f_{\rm ELM}$ can have significantly different $n_{\rm e}^{\rm ped}$. This suggests that the rate of change of the ELM particle losses might play only a small role in determining the pedestal density. Other mechanisms must be invoked to fully explain the difference in density between D and T plasmas.

8.2. Testing a pedestal density model

Very recently, a new predictive model for the pedestal density has been proposed [72]. Hereafter the new model will be called 'Saarelma-Connor model'. The Saarlema-Connor model extends the neutral penetration model [73] by including charge exchange processes in the pedestal [74] and allowing a core density gradient. The Saarelma-Connor model has several input parameters, among which the key ones are $n_{\rm e}^{\rm sep}$, $A_{\rm eff}$ and the ratio $\chi_{\rm e}/D_{\rm e}$ (where $D_{\rm e}$ is the electron particle diffusivity).

Due to the wider set of input parameters, the Saarelma-Connor model can predict the experimental density more accurately than the neutral penetration model. In particular, it is able to predict the lower pedestal density that characterizes the hydrogen plasmas compared to the deuterium plasmas, as recently shown in [72]. Interestingly, the neutral penetration alone gives a trend opposite to that experimentally observed, as also pointed out in the comparison of H and D type I ELMy H-mode pedestals in [26]. As the particle velocity scales as $v \sim \sqrt{1/M_i}$, the neutral penetration model predicts a decrease of the pedestal density with increasing isotope mass, opposite to what is observed experimentally. However, in the Saarelma-Connor model, $n_{\rm e}^{\rm sep}$ and χ/D are input parameters, so they can be adjusted to have a match between predicted and experimental density.

The goal of this subsection is to test, from a qualitative point of view, the predictions of the Saarelma-Connor model for the $A_{\rm eff}$ scan dataset and identify under which conditions of the input parameters we can obtain reasonable predictions.

Figure 21(*a*) shows the experimental $n_{\rm e}^{\rm ped}$ (the coloured dots) along with the model predictions (black lines). Initially, the model has been run assuming $\chi_{\rm e}/D_{\rm e} = 0.5$ and using the experimental $n_{\rm e}^{\rm sep}$ for each $A_{\rm eff}$ value. The ratio $\chi_{\rm e}/D_{\rm e} = 0.5$ has been chosen so that the density of the deuterium plasmas

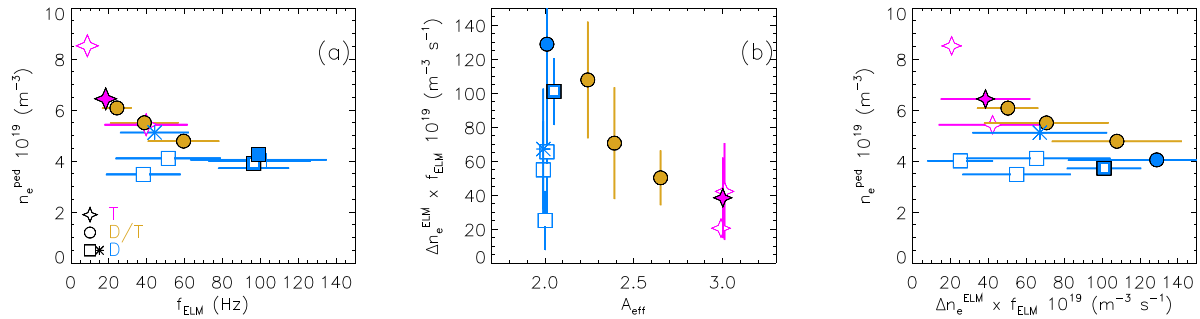

Figure 20. (*a*) Electron pedestal density versus ELM frequency. (*b*) Estimate of the rate of particles lost during ELMs versus $A_{\rm eff}$. (*c*) Pedestal density versus the rate of particles lost during ELMs. The full symbols with the black outline highlight the $A_{\rm eff}$ scan dataset while the open symbols highlight the extended dataset.

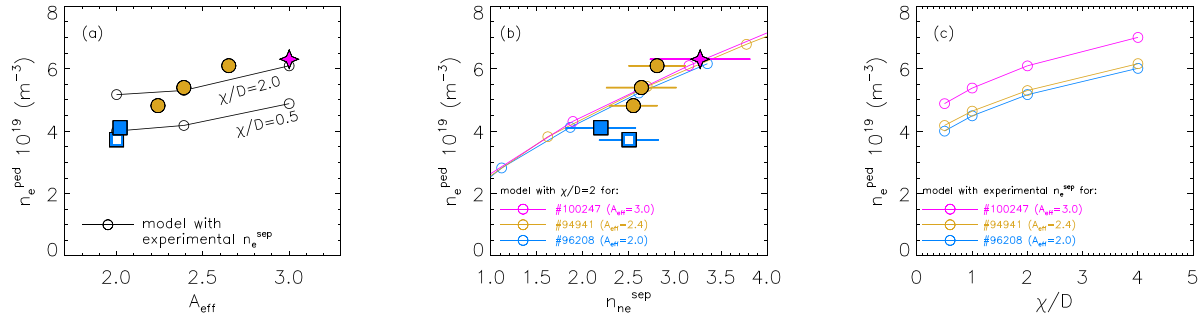

Figure 21. Pedestal density versus (*a*) $A_{\rm eff}$, (*b*) separatrix density and (*c*) ratio χ/D. The coloured full circles are the experimental data while the lines highlight the predictions from the Saarelma-Connor model.

are reasonably predicted. The increase of $A_{\rm eff}$ in the model (at constant $\chi_{\rm e}/D_{\rm e}$) leads to a clear but weak increase in $n_{\rm e}^{\rm ped}$. This is qualitatively consistent with the experimental results and with the modelling results for hydrogen and deuterium plasmas discussed in [72]. The increase in the predicted $n_{\rm e}^{\rm ped}$ is clearly due to the fact that the experimental $n_{\rm e}^{\rm sep}$ is an input parameter and that $n_{\rm e}^{\rm sep}$ increases with increasing $A_{\rm eff}$, as earlier shown in figure 11(*a*). Indeed, the model has a strong dependence on $n_{\rm e}^{\rm sep}$, as shown in figure 21(*b*) and clearly discussed in [72].

From a quantitative point of view, the density prediction at $\chi_{\rm e}/D_{\rm e} = 0.5$ under predicts the density of the T pulse. A better agreement can be obtained by increasing $\chi_{\rm e}/D_{\rm e}$, as shown in figure 21(*a*) by the upper black line. Assuming $\chi_{\rm e}/D_{\rm e} = 2.0$, the density of the T pulse is well predicted and the same qualitative trend between $n_{\rm e}^{\rm ped}$ and $A_{\rm eff}$ is obtained, but the deuterium pulse is now over predicted. Indeed, as shown in figure 21(*c*) the model predicts higher $n_{\rm e}^{\rm ped}$ with increasing $\chi_{\rm e}/D_{\rm e}$.

In conclusion, the results show that the Saarelma-Connor model can qualitatively predict the increase of the pedestal density with increasing $A_{\rm eff}$ if the experimental separatrix density is used as input. From a quantitative point of view, good $n_{\rm e}^{\rm ped}$ predictions in both D and T plasmas can be achieved only assuming that the T plasma has higher $\chi_{\rm e}/D_{\rm e}$ than the D plasma, i.e. assuming that the particle transport in tritium is lower than in deuterium. Assuming that the model is reliable, this might be considered as an indirect evidence that the particle transport in T plasma is lower than in D plasmas. More discussion on this point will be presented in section 11.

9. Microinstabilities in the pedestal of the deuterium tritium mass scan

A recent gyrokinetic study in the pedestal of selected JET-ILW hydrogen and deuterium type I ELMy H-modes has shown a significant effect of the isotope mass on the inter-ELM turbulent particle transport [30]. While no significant effect was observed on the large wavenumber modes ($\rho_{\rm e}$-scale) by using the hydrogen or the deuterium mass, a clear effect consistent with an anti-gyro-Bohm scaling was observed with the low wavenumber modes, at the $\rho_{\rm i}$-scale. Non-linear global simulations showed a reduction of the particle transport in the deuterium plasma compared to the hydrogen plasma. This was consistent with the experimentally observed increase of the pedestal density from hydrogen to deuterium [11, 26].

This section characterizes the micro-instabilities in the pedestal of the deuterium pulse #96208 and the T pulse #100247 (part of the $A_{\rm eff}$ scan dataset) by describing initial results of linear local and global GENE [75] gyrokinetic analysis. This is the first step of a long term project that in the future will be extended to the D/T pulses and to global non-linear simulations to assess the turbulent transport in the deuterium and tritium pedestals.

The profiles used in this work assume $T_{\rm e}^{\rm sep} = 100\,{\rm eV}$, for consistency with previous GENE analysis in JET-ILW. The work has initially assumed $T_{\rm i} = T_{\rm e}$ in the pedestal. As already described, this assumption is valid at the pedestal top while at the separatrix $T_{\rm i} > T_{\rm e}$ can be expected. For this reason, a sensitivity test on a possible $T_{\rm i}^{\rm sep}$ effect has been done using

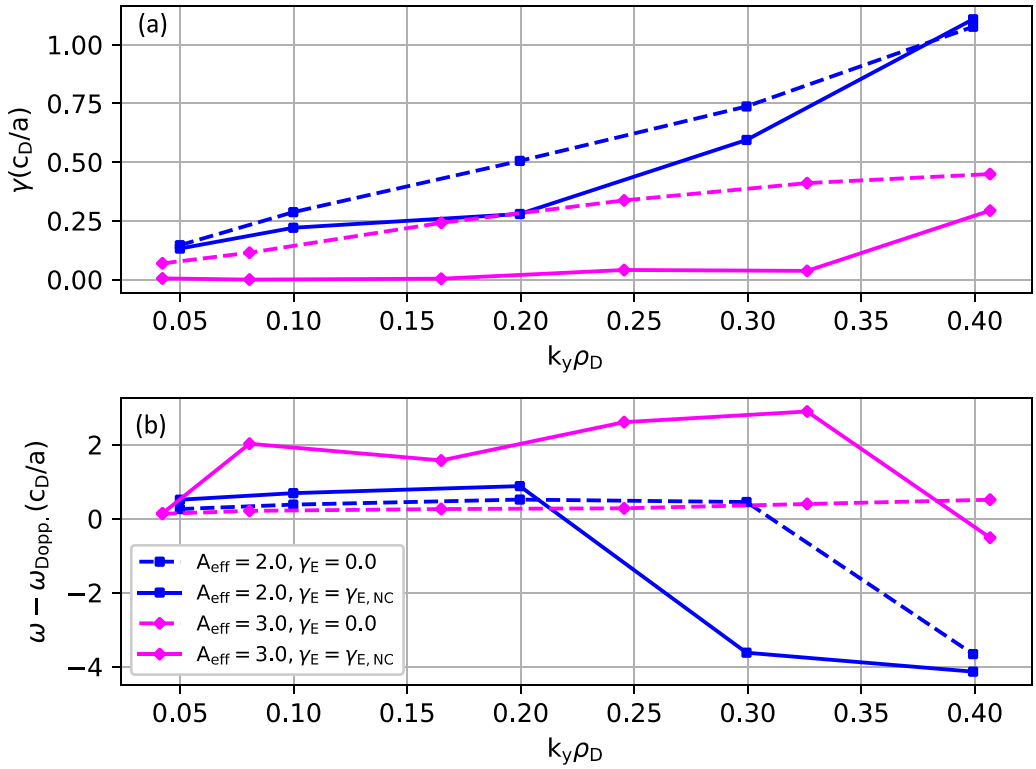

Figure 22. Global linear GENE simulations from D pulses #96208 (blue) and the T pulse #100247 (magenta) without (dashed lines) and with (continuous lines) flow shear. Frame (*a*) shows the growth rate and frame (*b*) the rotation frequency.

a modified T_i profile with $T_i^{ped} = T_e^{ped}$ and $T_i^{sep} = 400\,eV$ as upper bound.

Global simulations, which model the impact of profile variation [76], are more appropriate for the ion scale instabilities ($k_y\rho_D \leqslant 1$) which is thought to be important for the isotope effect [30]. For this reason, the local simulations are only briefly described and not discussed in any figure. Locally, a complex variety of different microinstabilities has been found in the pedestal. These include ion and electron temperature gradient modes (ITG and ETG) peaking both at and away from the outboard midplane, trapped electron modes (TEMs) and kinetic ballooning modes (KBMs).

The global simulations presented here model electron and ions dynamically, with impurities taken into account in the Landau collision operator via the experimentally estimated value of Z_{eff}. In the radial domain the simulation box spans $0.9375 < \rho_t < 0.9925$ with 480 cells. The buffer region in which the gradients are smoothly set to zero was set to 10% on the inner side of the domain, and on the outer side it was set to 5%–15% based on convergence tests. In the direction along the field line 84 gridpoints were used. In the velocity direction, $(v_\parallel, \mu) \in [-4v_{th}, 4v_{th}] \times [0, 11T/B]$ is resolved with 64×24 grid points.

The results of global computations assuming $T_i = T_e$ are shown in figure 22 both without flow shear (assuming $\gamma_E = 0$, dashed lines) and with equilibrium flow shear γ_E (solid lines). In this preliminary analysis, the equilibrium flow shear has been estimated using the neoclassical formula assuming $v_\parallel = 0$ [77, 78]. Note that the mass used in the normalisation of the quantities plotted in figure 22 is fixed to the deuterium

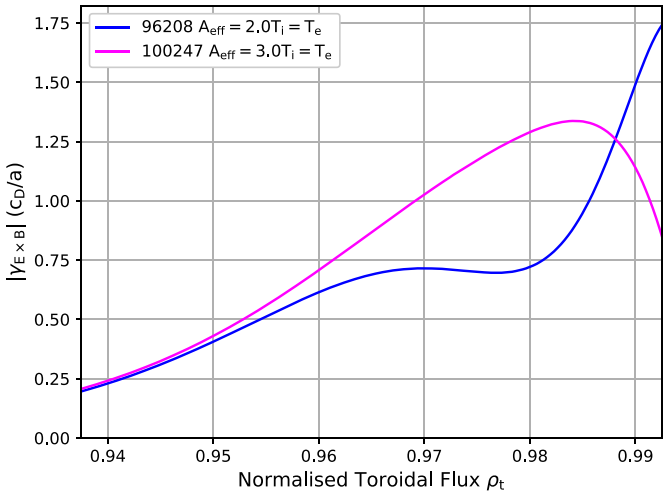

Figure 23. Neoclassical flow shear for the simulations of figure 22.

mass. Without flow shear (dashed lines), ITG/TEM growth rates are slightly lower in the T pulse (as can be seen by comparing the blue dashed line with the magenta dashed line). The inclusion of the flow shear amplifies significantly this difference. ITG/TEM are only partially suppressed by the equilibrium flow shear γ_E in the D pulse, as can be seen by comparing the blue dashed and solid lines. Instead, ITG/TEM are completely suppressed in the T pulse (magenta dashed and solid lines). This is due to the increase in $\gamma_{E,}$ across the radial domain, as shown in figure 23.

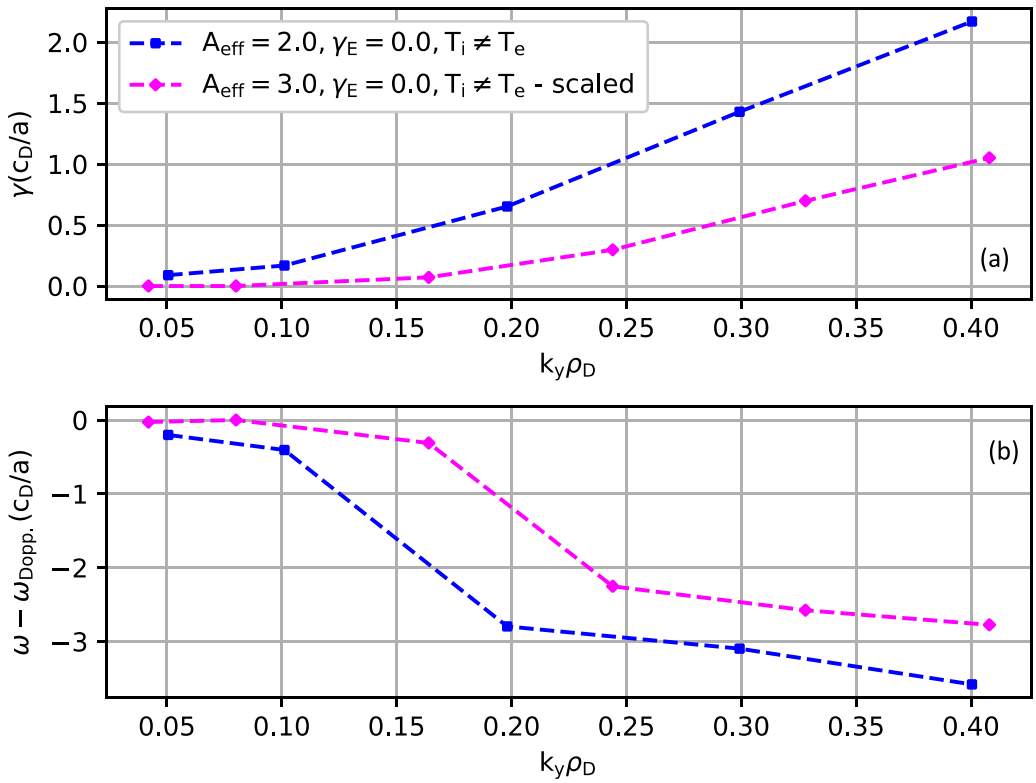

Figure 24. Global linear GENE simulations from D pulses #96208 (blue) and the T pulse #100247 (magenta) assuming $T_i^{sep} = 400$ eV. Frame (*a*) shows the growth rate and frame (*b*) the rotation frequency.

We note that no KBMs have been found in the global simulations, although their presence cannot be ruled out due to their large radial extent and the necessity to use Dirichlet boundary conditions close to the separatrix. The modes at $k_y\rho_D \gtrsim 0.3$ with frequency in the plasma frame $\omega\,(c_D/a) \sim -4$, see figure 22(*b*), are ETG modes with high radial wavenumber and do not appear to be affected by flow shear. These ETGs modes have a fine structure in the x-direction meaning $nx = 640$ is required in some cases to ensure adequate convergence.

The results of global GENE simulations (without flow shear) assuming $T_i \neq T_e$ are shown in figure 24. For precision, the gradient of T_i has been modified in order to have $T_i^{ped} = T_e^{ped}$ (as experimentally verified) and $T_i^{sep} = 400\,$eV. There are two notable differences from the corresponding $T_i = T_e$ simulations. First of all, ETG modes are now dominant across an extended range of $k_y\rho_D$ values. Second, the growth rates of the ETG modes are significantly higher. This is because ETG modes are sensitive to the value of $\tau = Z_{eff}T_e/T_i$. The decrease of τ tends to destabilize the ETG modes. Due to the higher T_i^{sep}, the value of T_i in the steep gradient region (where the drive is maximised and the instability therefore peaks) is larger than T_e, meaning τ is much smaller than the $T_i = T_e$ case. Therefore, ETG growth rates are indeed expected to be higher in the $T_i \neq T_e$ case. Note that this does not imply that the ITG/TEM modes are completely suppressed, only that they are now subdominant. Still, in the $T_i \neq T_e$ case it is expected the ITG/TEM growth rates to be lower due to the smaller value of normalised ion temperature gradient compared with the $T_i = T_e$ case. However, turning the attention to the comparison between the D pulse and T pulse, also in the $T_i \neq T_e$ case the growth rates of the microinstabilities is lower in the T pulse than in the D pulse.

No simulations with flow shear have been done for the $T_i \neq T_e$ case. Given the dominance of ETG modes and the expectation that they are unlikely to be significantly affected by equilibrium flow shear, we have decided not to perform counterpart simulations including flow shear at this time.

In conclusion, this gyrokinetic analysis has shown that the growth rates of the fastest growing microinstabilities are lower in the T pulse than in the D pulse, both for $T_i = T_e$ case and the $T_i \neq T_e$ case. This result in isolation does not allow us to comment on the possible difference in the turbulent transport, but it is a first step in the characterization of the pedestal properties in D and T. Ongoing nonlinear global simulations are needed to quantify the impact, if any, of these modes on turbulent transport.

10. Effect of isotope mass on pedestal stability

We now turn to discuss the impact of A_{eff} on the pedestal stability. Reliable pedestal predictions can be obtained only if the type I ELM triggering mechanism is fully understood. The most accepted mechanism is that ELMs are triggered once the PB modes are destabilized [31, 79]. In deuterium plasmas, the agreement between the PB model and the experimental results have been tested in a large variety of experimental conditions and devices. While initial results showed

reasonable agreements between ideal MHD and the experimental results in several machines, including JET-C [55] (and at low gas rate also JET-ILW [5, 80]), a satisfactory agreement was not always achieved in JET-ILW [4] in particular at high power and high gas rate [5]. This disagreement has been systematically investigated in several studies [33–36, 51] and it has been empirically correlated with the relative shift between density and temperature position (which is, in turn, correlated to n_e^{sep}/n_e^{ped}). The key idea is that increase of n_e^{sep}/n_e^{ped} leads to an increase in the pedestal turbulent transport that reduces the temperature gradient and makes resistive effects non-negligible [36, 81]. Indeed, the use of resistive MHD has led to a much better agreement with the experimental data [81], even if further physics effects (such as finite Larmor radius effects and a proper treatment of the diamagnetic stabilization [10, 58, 59]) are likely necessary to reach a perfect agreement with experiment.

In terms of effect of the isotope mass, a recent work has shown that ideal MHD was not sufficient to explain the difference in the pedestal stability between hydrogen and deuterium type I ELMy H-mode plasmas [26]. The problem was twofold. First of all, the pre-ELM pedestal of the hydrogen plasma was stable to ideal PB modes. Second, the effect of the isotope mass on the ideal stability of the PB modes was minimal. This second point requires a short discussion. The PB stability can be assessed with two criteria, the Alfven criterion and the diamagnetic criterion. With the Alfven criterion, PB modes are defined unstable when the normalized growth rate is $\gamma/\omega_A > 0.03$, where ω_A is the Alfven frequency. The PB growth rate γ and ω_A have the same dependence on the isotope mass $\left(A^{-1/2}\right)$, so the pedestal stability determined with the Alfven criterion is not affected by the isotope mass. With the diamagnetic criterion, PB modes are unstable when the growth rate is $\gamma/\omega^*_{max} > 0.25$, where ω^*_{max} is the maximum diamagnetic frequency in the pedestal. ω^*_{max} has no dependence on the isotope mass, so the PB stability determined with this criterion can be affected by A_{eff}. As already mentioned, this effect is small using ideal MHD and does not explain the difference in the pre-ELM pressure gradients between hydrogen and deuterium plasmas [26].

This section characterizes the PB stability of the A_{eff} scan dataset. First, the effect of the isotope mass on the PB stability is assessed with ideal MHD, reaching results consistent with those described for hydrogen and deuterium in [26, 27]. Then, the effect of the isotope mass is assessed with resistive MHD. The results with resistive MHD show qualitative agreement with the experimental results, suggesting that the resistive effects are important to assess properly the impact of the isotope mass on the pedestal.

The following numerical results have been determined with the linear resistive MHD stability code CASTOR [82] using the approach described in detail in [81]. The ideal stability part has been benchmarked with MISHKA [83] leading to the same conclusions. The equilibrium is determined with HELENA [84], a fixed boundary equilibrium solver that takes in input the fit to the experimental data and uses the bootstrap current determined with the Redl formula [85]. To remove possible uncertainties in the absolute position of temperature and density, the profiles used in the stability analysis have been radially shifted to the electron temperate at the separatrix determined by the two point model, as discussed in section 3.2. Given the good quality of the equilibrium, the radial shift is less than 0.5 cm. A sensitivity test has been performed for the key simulations to assess the difference between this approach and the standard assumption $T_e^{sep} = 100\,eV$ (the value typically used in JET-ILW PB stability analysis). The result of the sensitivity test is that the two approaches do not lead to any significant difference, as already shown for many other datasets in JET-ILW [36, 81]. Moreover, the following results have assumed $T_i = T_e$. As already discussed, this assumption is valid at the pedestal top while at the separatrix $T_i^{sep} > T_e^{sep}$ can be expected. For this reason, a sensitivity test has been carried out using a modified T_i profile with $T_i^{ped} = T_e^{ped}$ and $T_i^{sep} = 400\,eV$ as extreme upper bound. The sensitivity test shows that the quantitative results have only a slight difference from the standard $T_i = T_e$ case. From a qualitative point of view, no difference was observed. A sensitivity test has been performed also for Z_{eff} showing that a variation in the range $Z_{eff} = 1.2 - 2.0$ cannot affect the conclusion of the work.

Since the Alfven criterion cannot predict any effects of the isotope mass on the pedestal stability, all the following results have been obtained using the diamagnetic criterion.

10.1. Ideal MHD

The PB stability diagram in $j - \alpha$ space determined with ideal MHD for the T pulse #100247 is shown in figure 25(*a*) with the continuous magenta line. The *y*-axis in figure 25(*a*) is the maximum current density in the pedestal $j_{edge,max}$ normalized to the average current density j, while the *x*-axis is the normalized maximum pressure gradient α defined in [86]. The ideal PB stability has been determined with the CASTOR code using zero resistivity. The experimental pre-ELM values, α_{exp} and j_{exp}, are shown by the magenta star. The experimental pre-ELM pedestal is rather close to the PB stability but, being located to the left of the stability boundary, still slightly stable to ideal PB modes. The level of agreement between the PB stability and the experimental pre-ELM profiles is quantified as shown in figure 25(*b*). The thick continuous line in figure 25(*b*) shows the growth rates of the most unstable PB modes as function of α. The growth rates have been determined at constant j, using the $j_{edge,max}/\langle j \rangle$ of the experimental pedestal. The predicted normalized pressure gradient α_{crit} is determined using the diamagnetic criterion as the α value at which $\gamma/\omega^*_{max} = 0.25$. As reference, the vertical thin magenta line shows the value of α_{exp} and the shaded magenta area its uncertainty. Ideal MHD overestimates the experimental pressure gradient only by a factor $\alpha_{crit}/\alpha_{exp} \approx 3.2/2.7 = 1.18$, so for the T pulse ideal MHD and experimental results are in agreement within a 20% uncertainty.

As reference, the blue empty square in the figure 25(*a*) and the blue area in figure 25(*b*) show the pre-ELM experimental values of the D pulse #96208.

To assess the effect of the isotope mass on the stability, the same procedure has been repeated using the same input

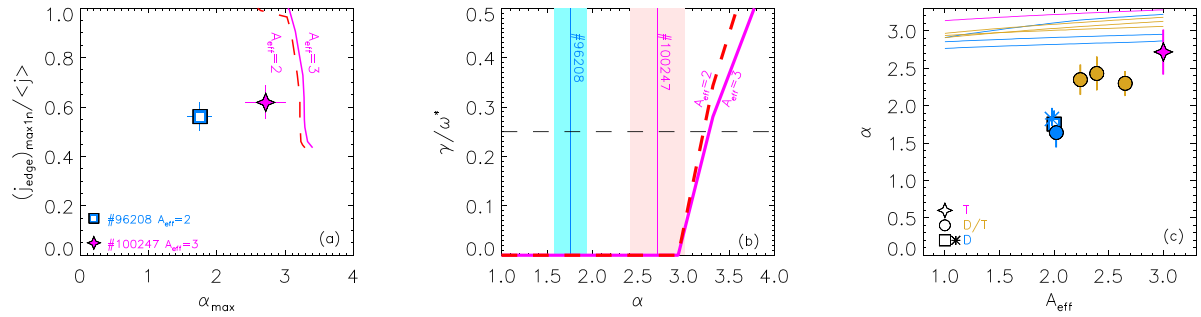

Figure 25. Ideal MHD stability results. (*a*) Stability boundary for the T pulse, first using $A_{\rm eff}=3$ (continuous line) and then assuming $A_{\rm eff}=2$ (dashed line). The star and square highlight the experimental α and j of the T pulse #100247 (magenta) and the D pulse #96208 (blue). (*b*) Growth rates versus α determined at the experimental j, for the T pulse, first using $A_{\rm eff}=3$ and then assuming $A_{\rm eff}=2$. The shaded areas and the continuous lines highlight the experimental α of the D and T pulses. (*c*) Experimental α (data points) and critical alpha (lines) versus $A_{\rm eff}$.

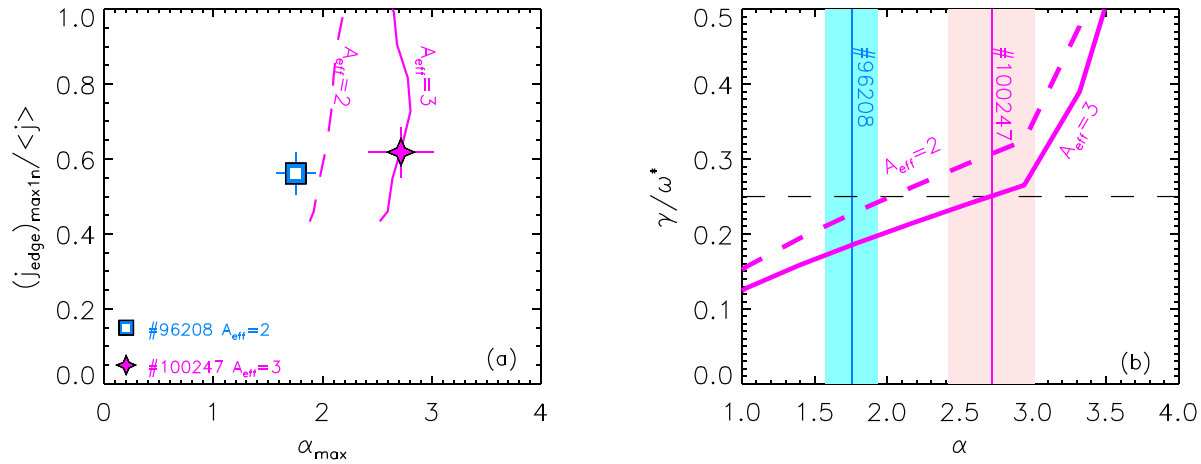

Figure 26. Resistive MHD stability results. (*a*) Stability boundary for the T pulse, first using $A_{\rm eff}=3$ (continuous line) and then assuming $A_{\rm eff}=2$ (dashed line). The star and the square highlight the experimental α and j of the T pulse (magenta) and the D pulse (blue). (*b*) Growth rate versus α determined at the experimental j, for the T pulse, first using $A_{\rm eff}=3$ and then assuming $A_{\rm eff}=2$. The shaded areas and the continuous lines highlight the experimental α of the D and T pulses.

parameters but using $A_{\rm eff}=2$ for the isotope mass. The corresponding stability boundary is shown in figure 25(*a*) with a dashed line. The effect of the isotope mass on the ideal PB stability boundary is small and similar to what obtained in H and D plasmas in [26]. The corresponding $\alpha_{\rm crit}$ has been determined in figure 25(*b*), showing a negligible difference from the case with $A_{\rm eff}=3$. The effect is small because the curve γ versus α is rather steep, so only large variations in γ can lead to significant variations in $\alpha_{\rm crit}$. Moreover, the growth rates scale as $(A_{\rm eff})^{-0.5}$, so only a 22% difference is expected in the growth rates between D and T plasmas.

The approach described in figure 25(*b*) has been repeated varying $A_{\rm eff}$ in the range 1–3. The corresponding $\alpha_{\rm crit}$ versus $A_{\rm eff}$ is shown in figure 25(*c*) by the magenta line, along with all the $\alpha_{\rm exp}$ determined for the experimental $A_{\rm eff}$ scan dataset. Clearly, $\alpha_{\rm exp}$ increases with increasing $A_{\rm eff}$, while $\alpha_{\rm crit}$ does not show any strong dependence on $A_{\rm eff}$.

To strengthen this statement, this type of analysis has been repeated for all the experimental data of the $A_{\rm eff}$ scan dataset. The results are summarized in figure 25(*c*) with continuous lines. None of the results shows a strong effect of $A_{\rm eff}$ on $\alpha_{\rm crit}$. Moreover, the pre-ELM D/T pedestals and especially the pre-ELM D pedestals are significantly stable to ideal PB modes with $\alpha_{\rm crit}/\alpha_{\rm exp}\approx 2$ for the D pulse #96208.

In conclusion, ideal MHD cannot explain the effect of the isotope mass on the pedestal stability of this dataset.

10.2. Resistive MHD

An analysis similar to that done for ideal MHD has been repeated using resistive MHD with resistivity determined from the Sptizer formula and the experimental $T_{\rm e}$ profiles.

The resistive PB stability diagram is shown in figure 26(*a*) for the T pulse #100247. The experimental point is on the stability boundary, showing that in the T pulse the ELMs are triggered once the resistive MHD stability boundary is reached. The analysis has been repeated by changing only the value of the isotope mass, from $A_{\rm eff}=3$ (continuous line) to $A_{\rm eff}=2$ (dashed line). The effect of the isotope mass on the stability boundary is significant and using $A_{\rm eff}=2$ the stability boundary moves very close to the experimental deuterium data point. The effect is consistent with the experimental difference in $\alpha_{\rm exp}$ between the D pulse and the T pulse.

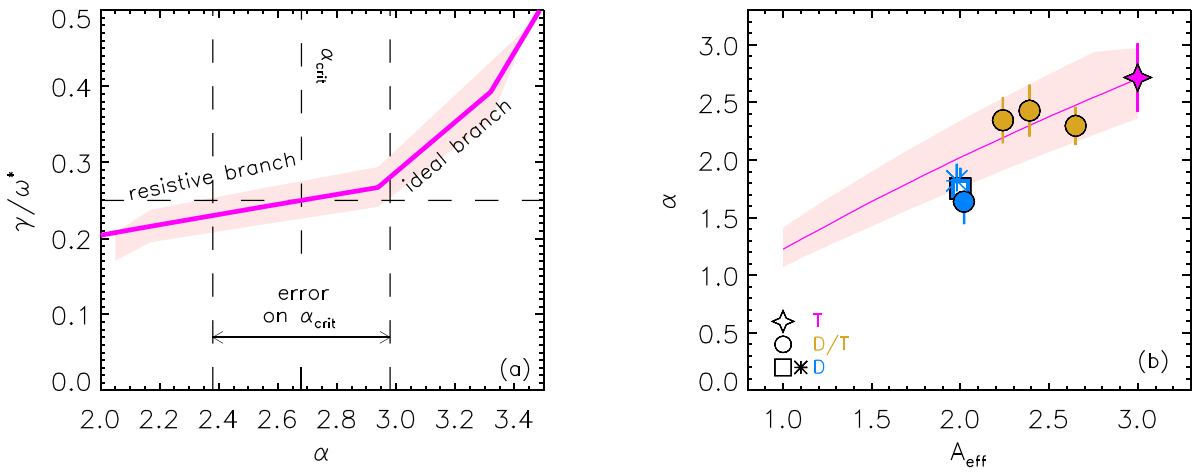

Figure 27. Resistive MHD stability results. (*a*) Growth rate versus α determined at the experimental j for the T pulse. The shaded areas highlight the variation in the growth rate due to the uncertainty in ω^*. (*b*) Experimental α (data points) and critical alpha (line) versus $A_{\rm eff}$.

The reason for the difference between ideal and resistive MHD can be explained via figure 26(*b*), where $\gamma/\omega^*_{\rm max}$ versus α is shown. In figure 26(*b*) the growth rates have been determined using the $j_{\rm edge,max}/\langle j\rangle$ of the T pulse. This type of diagram has been discussed in details in [81]. Here, we simply note that two behaviours can be observed. First, above $\alpha \approx 3$, the growth rates increase significantly with increasing α. These are ideal PB modes. This part of the diagram will be named 'ideal branch', as shown in figure 27(*a*). Below $\alpha \approx 3$, the growth rates show only a weak increase with increasing α. These modes are destabilized by resistivity (and might be resistive interchange modes [87], as discussed in [81]). This part of the diagram will be named 'resistive branch', see also figure 27(*a*). Since the slope of γ versus α is rather low in the resistive branch, a small variation in γ can lead to a significant change in $\alpha_{\rm crit}$.

At this stage, it is important to mention that the determination of $\alpha_{\rm crit}$ has a larger uncertainty in the resistive branch than in the ideal branch. This is because, due to the different slopes, small variations in γ can lead to larger variation in $\alpha_{\rm crit}$ in the resistive branch than in the ideal branch. An initial assessment of this uncertainty has been attempted in figure 27. For simplicity, only the uncertainty in ω^* has been considered. This was done using the approach described in section 7.3 using the uncertainty on the fits to the experimental $T_{\rm e}$ and $n_{\rm e}$ profiles. The shaded areas in figure 27(*a*) show the corresponding range of variation of $\gamma/\omega^*_{\rm max}$, while the thick line shows the average. $\alpha_{\rm crit}$ has been determined as the intersection of the thick line with the critical threshold $\gamma/\omega^*_{\rm max} = 0.25$. The uncertainty on $\alpha_{\rm crit}$ has been determined as the intersection of the boundaries of the shaded areas with 0.25. For the example of figure 27(*a*), corresponding to the T pulse #100247, the result is $\alpha_{\rm crit} = 2.7 \pm 0.3$. More proper and precise estimates of the uncertainty on $\alpha_{\rm crit}$ will be kept as future work.

This method to estimate $\alpha_{\rm crit}$ and its uncertainty has been repeated using different values of $A_{\rm eff}$, providing the predicted effect of the isotope mass on $\alpha_{\rm crit}$ and its uncertainty. The result is summarized in figure 27(*b*) along with the experimental data points of the $A_{\rm eff}$ scan dataset. The agreement between $\alpha_{\rm crit}$ and the experimental results is, within the uncertainty, remarkable. The result of figure 27(*b*) shows that resistive MHD can significantly contribute to understanding the effect of the isotope mass on the pedestal stability.

To strengthen this statement, the same approach has been repeated for all the experimental data of the $A_{\rm eff}$ scan dataset. The results are summarized in figure 28, without the uncertainties on $\alpha_{\rm crit}$ for the sake of clarity. The results for the D/T pedestal are approximately similar to that obtained for the T pedestal. Unfortunately, $\alpha_{\rm crit}$ is underestimated for the D pulses. This disagreement might be related to the fact that finite Larmor radius effects and the diamagnetic stabilization are not properly treated. It could also be related to uncertainty in the experimental data. As shown in figure 27(*b*), the uncertainty is rather large, so the disagreement is less strong that how it looks from figure 28(*a*). However, it is worth to mention that all the numerical results of figure 28(*a*) are in good qualitative agreement with the experimental data. First of all, all the modelled results shows a positive correlation between $\alpha_{\rm crit}$ and $A_{\rm eff}$. Second, the relative variation of $\alpha_{\rm crit}$ with $A_{\rm eff}$ is strong in all the modelled cases, as shown in figure 28(*b*). The relative variation of $\alpha_{\rm crit}$ between deuterium and tritium is significant and in the range 20%–40%.

Note that the resistive model predicts that the isotope mass continues to affect the stability also when comparing hydrogen and deuterium plasmas. As shown in figure 28(*b*), the variation in $\alpha_{\rm crit}$ from $A_{\rm eff} = 2$ to $A_{\rm eff} = 1$ is approximately 50%. So, the resistive PB model might have the capability of explaining the effect of the isotope mass also when comparing H and D plasmas. This investigation will be kept for future work.

It is extremely important to note that resistive MHD does not always predict a large effect of the isotope mass on the pedestal. Under certain conditions, the model can predict almost a negligible effect. This occurs when the experimental pedestal is limited by ideal PB modes and is located in the ideal branch. As discussed in section 10.1, a negligible effect of the isotope mass on the stability is predicted in the ideal branch. The effect of the isotope mass on the pedestal stability starts to be significant only once the growth rates of the resistive

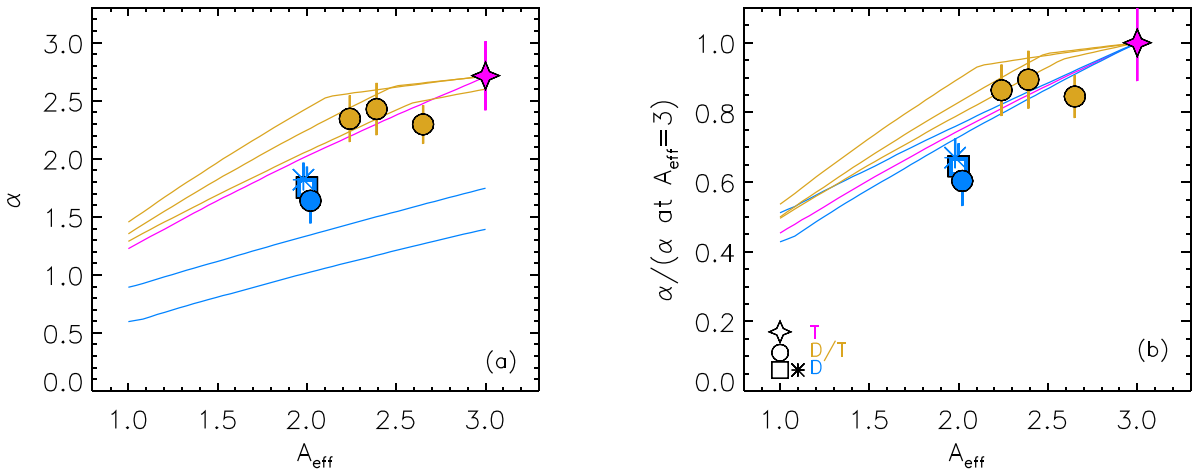

Figure 28. Resistive MHD stability results. (*a*) Experimental α (data points) and critical alpha (lines) versus $A_{\rm eff}$ for the entire $A_{\rm eff}$ scan dataset. Frame (*b*) shows the same results normalized to the $A_{\rm eff} = 3$ value to highlight the relative variation.

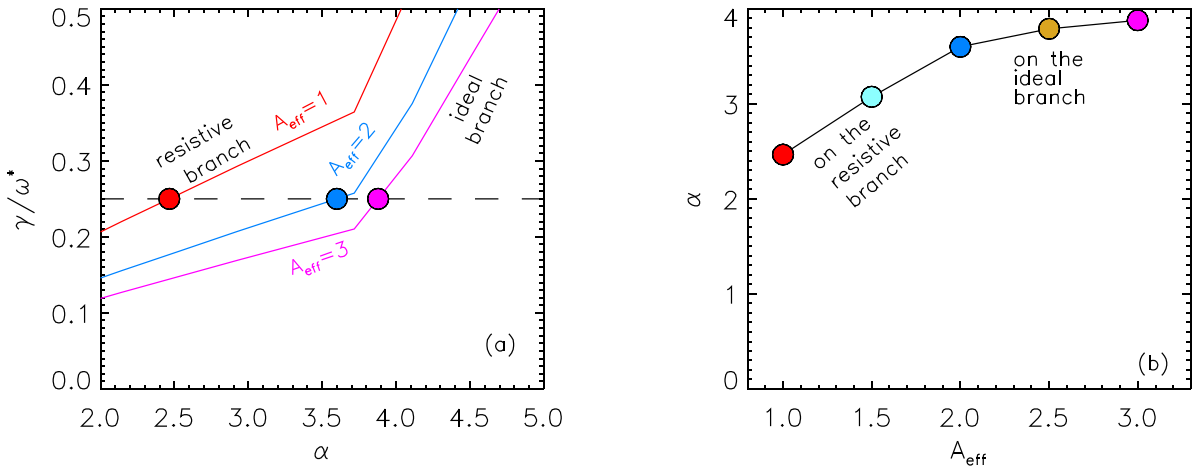

Figure 29. The figure sketch a possible difference in the effect of the isotope mass on the stability from the ideal branch to the resistive branch. If the pre-ELM pedestal is near the ideal branch, resistive MHD can predict a negligible effect on the stability. The analysis is done for the D pulse #87341, whose pedestal is close to the ideal MHD stability (the pulse is not included in the datasets discussed in this work).

modes becomes higher than the critical threshold. This idea is sketched in figure 29, where the stability analysis has been done for a D plasma selected to be limited by ideal MHD stability (#87341, a 1.4MA/1.7MA medium power and medium gas rate discharge [5] which is not included in the datasets discussed in this work). Figure 29(*a*) shows the growth rates versus α. For $\alpha < 3.5$, the growth rates have a weak dependence on $\alpha$and the most unstable modes are destabilized by resistivity. This is the resistive branch. For $\alpha > 3.5$, the growth rates have a stronger dependence on α. This is the ideal branch. The analysis has been repeated assuming several values of $A_{\rm eff}$, from 1 to 3. It is clear that in the example of figure 29(*a*), the difference in $\alpha_{\rm crit}$ is small from $A_{\rm eff} = 2$ to $A_{\rm eff} = 3$. This is due to two reasons. First of all, the effect on the MHD stability scales as $A^{-1/2}$, which leads to only a 22% variation on the growth rates. Second, the critical threshold is near the ideal branch where the strong correlation between γ and α implies that only large variation in the growth rates can lead to significant changes in $\alpha_{\rm crit}$. Instead, a significant difference in figure 29(*a*) can be seen for the cases from $A_{\rm eff} = 2$ to $A_{\rm eff} = 1$. This is again due to two reasons. Due to the square root dependence of the stability on $A_{\rm eff}$, from deuterium to hydrogen the growth rates scales by a 1.41 factor, which is larger than from D to T. Moreover, from $A_{\rm eff} = 2$ to $A_{\rm eff} = 1$ the critical threshold is at the resistive branch. So even small variations in γ can lead to significant changes in $\alpha_{\rm crit}$. The corresponding critical gradients are summarized in figure 29(*b*), where $\alpha_{\rm crit}$ versus $A_{\rm eff}$ is shown. In this example, no significant effect of the isotope mass on the pedestal stability is predicted in the range $2 < A_{\rm eff} < 3$, while the effect is significant in the range $1 < A_{\rm eff} < 2$. In different experimental conditions, it is reasonable to assume that the ideal branch might easily extend till hydrogen plasmas. This discussion shows that a strong effect of the isotope mass on the pedestal might not be a universal phenomenon. In principle, also negligible effects of the isotope mass on the pedestal stability can be expected. Indeed, the experimental results of JT-60U and DIII-D have shown no effect of the isotope mass on the pedestal [12–14, 29]. Minor effects in the pedestal structure have been observed also in a recent JET-ILW comparison between a D and D/T plasmas,

in which the pedestal was limited by ideal PB modes [88]. Finally, this observation could also explain the recent JET-ILW results discussed in [54] in which it is shown that at high gas rate (when resistive effects are likely relevant) a significant difference is observed in the pedestal between H, D and T plasma, while at low gas rate (when resistive effects are likely small) the difference is less evident.

11. Discussion and conclusions

This work has described the effect of the isotope mass on the pedestal using the unique results from the D/T campaign performed in JET-ILW in 2021–22. The key goal of the work was to assess the direct effect of the isotope mass on the pedestal stability. For this reason a specific $A_{\rm eff}$ scan at similar $\beta_{\rm N}$, $n_{\rm e}^{\rm sep}/n_{\rm e}^{\rm ped}$, $\nu^{*\rm ped}$, $\rho_i^{*\rm ped}$ has been performed. Keeping these parameters constant has allowed to avoid indirect effects of the isotope mass on the stability.

The work has discussed the pedestal structure, the pedestal transport from an experimental point of view, the pedestal microinstabilities and the pedestal stability.

In terms of pedestal structure, the key difference in the $A_{\rm eff}$ scan is due to the increase of the pedestal density from D to T plasmas. This seems a general result that has been observed also in other $A_{\rm eff}$ scans performed at constant power, in H plasmas, D plasmas and T plasmas with type I ELMs [11, 26, 27, 54]. The present results show that this is mainly due to an increase in the density gradient and not to a change in the pedestal width. This is consistent with the results recently obtained for a JET-ILW $A_{\rm eff}$ scan of type I ELMy pedestals at constant power and constant gas rate [54]. The results discussed in the present work suggest that the leading candidates to explain the experimental observations are changes in the pedestal stability and in the inter-ELM pedestal transport. In terms of pedestal stability, an improvement in the resistive MHD stability with increasing $A_{\rm eff}$ has been observed. In terms of pedestal inter-ELM heat transport, due to the large error bars, it was not possible to reach strong conclusions, however the experimental results might suggest a reduction of $\chi_{\rm eff}$ with increasing $A_{\rm eff}$. In terms of pedestal inter-ELM particle transport, no experimental results are available due to the large uncertainty in the particle source. Nonetheless, the strong increase of the density gradients with increasing $A_{\rm eff}$ suggests a possible reduction of the inter-ELM particle transport from D to T. This would be consistent with a recent gyrokinetic analysis in H and D plasmas which has shown a reduction of the particle inter-ELM transport from H to D [30]. A similar gyrokinetic analysis for the present $A_{\rm eff}$ scan is ongoing. However, we cannot exclude that a change in particle source from D to T plasmas can also play a role.

The work has shown that the type I ELM characteristics change across the present $A_{\rm eff}$ scan, with an increase of the ELM energy losses from D plasmas to the T plasma due to an increase in the convective losses. The origin of this behaviour is still unclear and cannot be explained by linear MHD. In the future, non-linear MHD studies will be necessary to identify the mechanism behind the increase of the convective losses.

A reasonable agreement between experimental results and resistive MHD has been obtained. However, a certain level of disagreement is still present, as shown in figure 28. In part, this could be due to uncertainties on the experimental profile. In part, this could be related to the fact some physics effects have not been properly considered. For example, experimental plasma rotation and a proper treatment of the diamagnetic stabilization are not possible with CASTOR. However, the toroidal rotation was very similar in the $A_{\rm eff}$ scan dataset, as shown in figure 12. Moreover, the inclusion of experimental rotation alone would not have changed the results significantly, as recently shown in JET-ILW with MISHKA [89]. On the other hand, the inclusion of plasma rotation together with the inclusion of the diamagnetic term might have an effect, as shown in [10, 58, 59]. An assessment of the combined effect of rotation and diamagnetic stabilization is kept for future work.

Nonetheless, the present qualitative agreement between resistive MHD and experimental results is extremely promising. In particular, it is worth to mention that resistive MHD predicts an effect of the isotope mass on the stability not only for D and T plasmas, but also for H and D plasma. It is likely that the results discussed in section 10.2, combined with a change in the inter-ELM transport [30], can explain the experimental difference observed in the pedestal of H and D pedestal of [11, 26]. The application of resistive MHD to H, D and Helium plasmas is kept for future work.

No predictive modelling has been attempted in this work. This is due to two reasons. Our present predictive capabilities are based on the EPED1 model [55], which has been implemented in the Europed code [90, 91]. The present implementation of the model assumes that the pedestal width scales accordingly to the empirical correlation used in EPED1 (the so called KBM constraint, which assumes $w_{\rm pe} = 0.076(\beta_\theta^{\rm ped})^{0.5}$ [55]) and employs ideal MHD to assess the pedestal stability of the PB modes. The present work has shown that neither the KBM constraint nor the ideal MHD are sufficient to describe the effect of the isotope mass on the pedestal width and stability. As shown in figure 9, the pedestal width in the $A_{\rm eff}$ scan is not consistent with the KBM constraint and, as shown in figure 25 (and already pointed out in [26]), ideal MHD does not predict any significant effect of the isotope mass on the pedestal stability. For these reasons, the present predictive model would not be able to describe correctly the pedestal behaviour in the $A_{\rm eff}$ scan. Presently, the predictive Europed code is under upgrade to include resistive MHD. Our capabilities of predicting the effect of isotope mass on the pedestal will be tested in the near future.

In conclusion, the work has described the effect of the isotope mass on the type I ELMy pedestal in an $A_{\rm eff}$ scan from D to T plasma. In terms of the pedestal structure, the key effect is an increase of the pedestal density due to an increase of the density gradient. From an experimental point view, the analysis of the parameter $\eta_{\rm e}$ suggests a reduction of the pedestal inter-ELM electron scale turbulent transport with increasing $A_{\rm eff}$. A likely candidate to explain the change in the pre-ELM density gradient is a reduction of the inter-ELM particle transport, as suggested by the fact that the changes in $\eta_{\rm e}$ are driven

only by the $\nabla n_e/n_e$ term. From a theoretical point of view, this is currently under investigation with a non-linear gyrokinetic analysis. The present results, based on linear analysis, indeed show a reduction in micro-instabilities growth rates from the D pulse to the T pulse. However, at this stage, a contribution due to the increase of the particle source from D plasmas to T plasmas cannot be excluded. Moreover, experimental results might suggest a reduction of the pedestal inter-ELM heat transport with increasing $A_{\rm eff}$. Unfortunately, due to the large uncertainties no strong conclusions on the pedestal $\chi_{\rm eff}$ are possible. Finally, the work shows that resistive MHD can qualitatively explain the effect of the isotope mass on the pedestal stability. This is an initial but important step towards the development of a predictive model for the impact of the isotope mass on the type I ELMy pedestal.

Acknowledgments

This research is supported by Vetenskapsrådet, under Grant No. 2019-04618.

This work has been carried out within the framework of the EUROfusion Consortium, funded by the European Union via the Euratom Research and Training Programme (Grant Agreement No. 101052200—EUROfusion). Views and opinions expressed are however those of the author(s) only and do not necessarily reflect those of the European Union or the European Commission. Neither the European Union nor the European Commission can be held responsible for them.

This scientific paper has been published as part of the international project co-financed by the Polish Ministry of Science and Higher Education within the programme called 'PMW' for 2022-2023.

ORCID iDs

L. Frassinetti https://orcid.org/0000-0002-9546-4494
C. Perez von Thun https://orcid.org/0000-0002-1166-2179
B. Chapman-Oplopoiou https://orcid.org/0000-0001-9879-2285
H. Nyström https://orcid.org/0000-0002-1310-4517
M. Poradzinski https://orcid.org/0000-0002-1858-4046
L. Horvath https://orcid.org/0000-0002-5692-6772
C.F. Maggi https://orcid.org/0000-0001-7208-2613
A. Stagni https://orcid.org/0000-0001-8084-1544
A. Chomiczewska https://orcid.org/0000-0003-4931-728X
R.B. Morales https://orcid.org/0000-0003-0667-3356
A.R. Field https://orcid.org/0000-0003-0671-9668
H.J. Sun https://orcid.org/0000-0003-0880-0013
B. Labit https://orcid.org/0000-0002-0751-8182
D.I. Refy https://orcid.org/0000-0002-0846-8236
P.A. Schneider https://orcid.org/0000-0001-7257-3412
E.R. Solano https://orcid.org/0000-0002-4815-3407
N. Vianello https://orcid.org/0000-0003-4401-5346
M. Vécsei https://orcid.org/0000-0003-4596-1211

References

[1] Scott S.D. *et al* 1995 *Phys. Plasmas* **2** 2299
[2] Jacquinot J. (JET Team) 1999 *Nucl. Fusion* **38** 1263
[3] Matthews G. *et al* 2013 *J. Nucl. Mater.* **438** S2
[4] Beurskens M. *et al* 2014 *Nucl. Fusion* **54** 043001
[5] Maggi C. *et al* 2015 *Nucl. Fusion* **55** 113031
[6] Nunes I. 2016 *Plasma Phys. Control. Fusion* **58** 014034
[7] Giroud C. *et al* 2013 *Nucl. Fusion* **53** 113025
[8] Giroud C. *et al* 2015 *Plasma Phys. Control. Fusion* **57** 035004
[9] Giroud C. *et al* 2016 Progress in understanding the role of low Z impurity in the confinement in JET ILW and in JET C plasmas *2016 IAEA Fusion Energy Conference* (*Kyoto 17–22 October 2016*) p EX/P6–13 (available at: https://nucleus.iaea.org/sites/fusionportal/Shared%20Documents/FEC%202016/fec2016-preprints/preprint0344.pdf)
[10] Giroud C. *et al* 2018 Optimisation of JET-DT and ITER operation by developing an understanding of the role of low-Z impurity on the H-mode pedestal *2018 IAEA Fusion Energy Conf.* (*Gandhinagar*, *22–27 October 2018*) p EX/3–4 (available at: https://nucleus.iaea.org/sites/fusionportal/Shared%20Documents/FEC%202018/fec2018-preprints/preprint0347.pdf)
[11] Maggi C.F. *et al* 2018 *Plasma Phys. Control. Fusion* **60** 014045
[12] Urano H., Takizuka T., Kamada Y., Oyama N. and Takenaga H. 2008 *Nucl. Fusion* **48** 045008
[13] Urano H., Takizuka T., Kikuchi M., Nakano T., Hayashi N., Oyama N. and Kamada Y. 2012 *Phys. Rev. Lett.* **109** 125001
[14] Urano H., Takizuka T., Aiba N., Kikuchi M., Nakano T., Fujita T., Oyama N., Kamada Y. and Hayashi N. 2013 *Nucl. Fusion* **53** 083003
[15] Schissel D.P. *et al* 1989 *Nucl. Fusion* **29** 185
[16] ASDEX Team 1989 *Nucl. Fusion* **29** 1959
[17] Bessenrodt-Weberpals M. *et al* 1993 *Nucl. Fusion* **33** 1205
[18] Laggner F. *et al* 2017 *Phys. Plasmas* **24** 56105
[19] Yamada H. *et al* 2019 *Phys. Rev. Lett.* **123** 185001
[20] Nagaoka K. *et al* 2019 *Nucl. Fusion* **59** 106002
[21] ITER Physics Basis 1999 *Nucl. Fusion* **39** 2175
[22] Cordey J.G. *et al* 1999 *Nucl. Fusion* **39** 301
[23] Maslov M., Boboc A., Brix M., Flanagan J.C., Peluso E., Price C. and Romanelli M. 2020 *Nucl. Fusion* **60** 036007
[24] Verdoolaege G. *et al* 2021 *Nucl. Fusion* **61** 076006
[25] Weisen H. *et al* 2020 *J. Plasma Phys.* **86** 905860501
[26] Horvath L. *et al* 2021 *Nucl. Fusion* **61** 046015
[27] Schneider P. *et al* 2022 *Nucl. Fusion* **62** 026014
[28] Schneider P., Hennequin P., Bonanomi N., Dunne M., Conway G.D. and Plank U. 2021 *Plasma Phys. Control. Fusion* **63** 064006
[29] Gohil P. *et al* "The H-mode power threshold, pedestal width and plasma transport in hydrogen plasmas in DIII-D" *2008 IAEA Fusion Energy Conf.* (*Geneve*, *13–18 October 2008*) p PD/P1–1
[30] Predebon I., Hatch D.R., Frassinetti L., Horvath L., Saarelma S., Chapman-Oplopoiou B., Görler T. and Maggi C.F. 2023 *Nucl. Fusion* **63** 036010
[31] Snyder P., Wilson H.R., Ferron J.R., Lao L.L., Leonard A.W., Osborne T.H., Turnbull A.D., Mossessian D., Murakami M. and Xu X.Q. 2002 *Phys. Plasmas* **9** 2037
[32] Dunne M. *et al* 2017 *Plasma Phys. Control. Fusion* **59** 025010
[33] Stefanikova E. *et al* 2018 *Nucl. Fusion* **58** 056010
[34] Stefanikova E., Frassinetti L., Saarelma S., Perez von Thun C. and Hillesheim J.C. (JET Contributors) 2021 *Nucl. Fusion* **61** 026008
[35] Frassinetti L. *et al* 2021 *Nucl. Fusion* **61** 016001
[36] Frassinetti L. *et al* 2021 *Nucl. Fusion* **61** 126054
[37] Frassinetti L. *et al* 2017 *Nucl. Fusion* **57** 016012

[38] Frassinetti L. *et al* 2017 *Plasma Phys. Control. Fusion* **59** 014014
[39] Versloot T.W. *et al* 2011 *Nucl. Fusion* **51** 103033
[40] Pasqualotto R., Nielsen P., Gowers C., Beurskens M., Kempenaars M., Carlstrom T. and Johnson D. 2004 *Rev. Sci. Instrum.* **75** 3891
[41] Refy D.I., Réfy D.I., Brix M., Gomes R., Tál B., Zoletnik S., Dunai D., Kocsis G., Kálvin S. and Szabolics T. 2018 *Rev. Sci. Instrum.* **89** 043509
[42] King D. *et al* 2020 *Nucl. Fusion* **60** 096030
[43] Maslov M. *et al* 2023 *Nucl. Fusion* **63** 112002
[44] Brezinsek S. *et al* 2013 *Nucl. Fusion* **53** 083023
[45] Matveev D. *et al* 2023 *Nucl. Fusion* **63** 112014
[46] Frassinetti L., Beurskens M.N.A., Scannell R., Osborne T.H., Flanagan J., Kempenaars M., Maslov M., Pasqualotto R. and Walsh M. 2012 *Rev. Sci. Instrum.* **83** 013506
[47] Groebner R.J. *et al* 2001 *Nucl. Fusion* **41** 1789
[48] Szepesi G. *et al* 2021 Advanced equilibrium reconstruction for JET with EFIT++ *47th EPS Conf. Plasma Physics* (*Stiges, Spain (virtual conference), 21–25 June 2021*) P 3.1037 (available at: http://ocs.ciemat.es/EPS2021PAP/pdf/P3.1037.pdf)
[49] Stangeby P.C., Canik J.M., Elder J.D., Lasnier C.J., Leonard A.W., Eldon D., Makowski M.A., Osborne T.H. and Grierson B.A. 2015 *Nucl. Fusion* **55** 093014
[50] Eich T. *et al* 2013 *Nucl. Fusion* **53** 093031
[51] Frassinetti L. *et al* 2019 *Nucl. Fusion* **59** 076038
[52] TRANSP group in Princeton Plasma Physics Laboratory *TRANSP Hompage* (available at: http://w3.pppl.gov/transp/)
[53] Hawryluk R. 1979 An empirical approach to tokamak transport *Physics of Plasmas Close to Thermonuclear Conditions Proc. of the Course Held in Varenna* (*Italy, 27 August–8 September 1979*) pp 19–46
[54] Schneider P. *et al* 2023 *Nucl. Fusion* **63** 112010
[55] Snyder P.B., Groebner R.J., Hughes J.W., Osborne T.H., Beurskens M., Leonard A.W., Wilson H.R. and Xu X.Q. 2011 *Nucl. Fusion* **51** 103016
[56] Sheikh U., Dunne M., Frassinetti L., Blanchard P., Duval B.P., Labit B., Merle A., Sauter O., Theiler C. and Tsui C. 2019 *Plasma Phys. Control. Fusion* **61** 014002
[57] Makarov S.O., Coster D.P., Kaveeva E.G., Rozhansky V.A., Senichenkov I.Y., Veselova I.Y., Voskoboynikov S.P., Stepanenko A.A., Bonnin X. and Pitts R.A. 2023 *Nucl. Fusion* **62** 026014
[58] Aiba N. *et al* 2017 *Nucl. Fusion* **57** 126001
[59] Aiba N. *et al* 2018 *Nucl. Fusion* **60** 014032
[60] Frassinetti L. *et al* 2015 *Nucl. Fusion* **55** 023007
[61] Loarte A. *et al* 2003 *Plasma Phys. Control. Fusion* **45** 1549
[62] Field A. *et al* 2020 *Plasma Phys. Control. Fusion* **62** 055010
[63] Goldston R., McCune D.C., Towner H.H., Davis S.L., Hawryluk R.J. and Schmidt G.L. 1981 *J. Comput. Phys.* **43** 61
[64] Brambilla M. 2002 *Plasma Phys. Control. Fusion* **44** 2423
[65] Horvath L. *et al* 2023 *Plasma Phys. Control. Fusion* **65** 044003
[66] de la Cal E. *et al* 2020 *Plasma Phys. Control. Fusion* **62** 035006
[67] Chapman B. *et al* 2022 *Nucl. Fusion* **62** 086028
[68] Field A. *et al* 2022 *Phil. Trans. R. Soc.* A **381** 2242
[69] Scott B. D. and Scott B.D. 2005 *Phys. Plasmas* **12** 062314
[70] Eich T., Manz P., Goldston R.J., Hennequin P., David P., Faitsch M., Kurzan B., Sieglin B. and Wolfrum E. 2020 *Nucl. Fusion* **60** 056016
[71] Eich T., Sieglin B., Scarabosio A., Fundamenski W., Goldston R.J. and Herrmann A. 2011 *Phys. Rev. Lett.* **107** 215001
[72] Saarelma S., Connor J.W., Bilkova P., Bohm P., Field A.R., Frassinetti L., Fridstrom R. and Kirk A. 2023 *Nucl. Fusion* **63** 052002
[73] Groebner R., Mahdavi M.A., Leonard A.W., Osborne T.H., Porter G.D., Colchin R.J. and Owen L.W. 2002 *Phys. Plasmas* **9** 2134
[74] Mahdavi M.V., Mahdavi M.A., Maingi R., Groebner R.J., Leonard A.W., Osborne T.H. and Porter G. 2003 *Phys. Plasmas* **10** 3984
[75] Jenko F., Dorland W., Kotschenreuther M. and Rogers B.N. 2000 *Phys. Plasmas* **7** 1904
[76] Görler T., Lapillonne X., Brunner S., Dannert T., Jenko F., Merz F. and Told D. 2011 *J. Comput. Phys.* **230** 7053
[77] Landreman M., Landreman M. and Ernst D.R. 2012 *Plasma Phys. Control. Fusion* **54** 115006
[78] Hatch D.R. *et al* 2019 *Nucl. Fusion* **59** 086056
[79] Wilson H.R., Snyder P.B., Huysmans G.T.A. and Miller R.L. 2002 *Phys. Plasmas* **9** 1277
[80] Perez von Thun C. *et al* 2019 *Nucl. Fusion* **59** 056004
[81] Nyström H., Frassinetti L., Saarelma S., Huijsmans G.T.A., Perez von Thun C., Maggi C.F., Hillesheim J.C. and contributors J. 2023 *Nucl. Fusion* **62** 126045
[82] Kerner W., Kerner W., Goedbloed J.P., Huysmans G.T.A., Poedts S. and Schwarz E. 1998 *J. Comput. Phys.* **142** 271
[83] Mikhailovskii A.B. *et al* 1997 *Plasma Phys. Rep.* **23** 844
[84] Huysmans G.T.A. *et al* 1991 Computational physics *Proc. Int. Conf.* (*Amsterdam, The Netherlands*) (World Scientific)
[85] Redl A., Angioni C., Belli E. and Sauter O. 2021 *Phys. Plasmas* **28** 022502
[86] Miller R.L., Chu M.S., Greene J.M., Lin-Liu Y.R. and Waltz R.E. 1998 *Phys. Plasmas* **5** 973
[87] Furth H.P., Furth H.P., Killeen J. and Rosenbluth M.N. 1963 *Phys. Fluids* **6** 459
[88] Giroud *et al* Private communication
[89] Sos M. *et al* 2022 Evaluating the impact of plasma toroidal rotation on the pedestal stability with ELITE on JET *18th Int. workshop on H-mode Physics and Transport barriers* (*Princeton, 20–23 September 2022*) (available at: https://sites.google.com/pppl.gov/h-modeworkshop2022)
[90] Saarelma S., Challis C.D., Garzotti L., Frassinetti L., Maggi C.F., Romanelli M. and Stokes C. 2018 *Plasma Phys. Control. Fusion* **60** 014042
[91] Saarelma S., Frassinetti L., Bilkova P., Challis C.D., Chankin A., Fridström R., Garzotti L., Horvath L. and Maggi C.F. 2019 *Phys. Plasmas* **26** 072501